High-resolution imaging of fault zone structure along the creeping section of the Haiyuan Fault, NE Tibet, from data recorded by dense seismic arrays

Zhou Zhang[1,2], Yangfan Deng[1,2]*, Hongrui Qiu[3], Zhigang Peng[4], Jing Liu-Zeng[5]

[1]State Key Laboratory of Isotope Geochemistry, Guangzhou Institute of Geochemistry, Chinese Academy of Sciences, Guangzhou, 510640, China

[2]CAS Center for Excellence in Deep Earth Science, Guangzhou, 510640, China

[3]Earth, Atmospheric and Planetary Sciences, Massachusetts Institute of Technology, Cambridge, MA 02139, USA

[4]School of Earth and Atmospheric Sciences, Georgia Institute of Technology, Atlanta, GA, USA

[5]Institute of Surface-Earth System Science, Tianjin University, Tianjin, China

* Correspondence: yangfandeng@gig.ac.cn

Abstract: High-resolution imaging of fault zone structures is essential for understanding earthquake physics and fault mechanics. As a major left-lateral strike-slip fault in northeastern Tibet, fine structures of the damage zone in the creeping (Laohushan) section of the Haiyuan fault remain unclear. To resolve geometry and velocity reduction of the damage zone, we deployed a dense temporary network of 110 seismic stations around the creeping section of the Haiyuan fault. Travel time delays from teleseismic P arrivals suggest an ~1-km-wide low-velocity zone, likely illuminating a broader damage zone around the Haiyuan fault. A catalog is constructed for local earthquakes based on phase picks identified from a machine learning technique. The amplification of waveforms from these local events and waveform modeling of fault zone trapped waves indicate a narrower inner damage zone with depth-dependent width (ranging from 150 m to 50 m) that extends to a depth of ~4 km. These values are generally consistent with those found on other non-creeping faults in California, suggesting that these damage zone properties are not affected by fault slip behaviors at shallow depth. In addition, a clear bi-material velocity contrast across the fault is revealed by the analysis of teleseismic P arrivals. Assuming the contrast extends to a depth of 15 km, we find that P wave velocity is ~5% slower in the crustal block north of the fault. Our study shows that a temporary dense seismic network is effective in illuminating cross-fault velocity contrast and fault geometry.

Plain Language Summary: The Haiyuan fault is a major left-lateral strike-slip fault in northeastern Tibet and has hosted two destructive earthquakes (1920 Haiyuan and 1927 Gulang earthquake) in the past century. Along the Laohushan section of the Haiyuan fault, between rupture zones of these two earthquakes, shallow aseismic creep and repeating earthquakes have been detected using geodetic and seismic data. However, the structure of this creeping section is still poorly understood. Therefore, we deployed a dense array with 110 stations crossing the fault surface trace. A catalog with more local earthquakes during the one-month recording period is constructed and relocated using this dense array. Based on analyses of signals from nearby and distant earthquakes, we find a ~100-m-wide slower fault inner zone that can trap incoming seismic energy and a wider (~1-km-wide) low-velocity damage zone beneath the array. The inferred fault zone structure is consistent with those found along other non-creeping faults in California, suggesting damage zone properties are likely not controlled by fault slip behaviors at shallow depth. The resulting high-resolution fault zone image also helps improve ground motion prediction and rupture simulation in the Laohushan section of the Haiyuan fault.

1. Introduction

Crustal earthquakes reflect rapid slip of two rock bodies along active fault zones. While most slip and deformation occur within a very narrow fault core, additional geological, geophysical, geodetic methods and dynamic modeling have found a much wider zone with intensive cracks/fractures and damaged rocks that are called fault damage zones (e.g., Ben-Zion & Sammis, 2003; Kim et al., 2004; Manighetti et al., 2004; Mitchell & Faulkner, 2009; Choi et al., 2016; Torabi et al., 2020; Peng & Deng, 2022). Understanding the properties of damage zones around active faults has important implications for many aspects of earthquake physics and fault mechanics, such as the deformation processes associated with faulting (e.g. Chester et al., 1993; Schulz and Evans, 1998; Wilson et al., 2003), strain distribution and deformation history in a region (e.g. Scholz & Cowie, 1990; Walsh et al., 1991; Marrett & Allmendinger, 1992), earthquake rupture propagation and near-fault seismic hazards (e.g. Harris & Day, 1997; Kim & Sanderson, 2008; Manighetti et al., 2009; Choi et al., 2012; Huang et al., 2014; Perrin et al., 2016; Weng et al., 2016; Chen & Yang, 2020), and transportation of fluids in the crust (e.g. Geraud et al., 2006; Kim & Sanderson, 2010). Active fault damage zones have been probed through a variety of methods, including microstructural analysis, gravity inversions, geodetic inversions based on Interferometric Synthetic Aperture Radar (InSAR) and GPS observations, air gun source, seismic tomography with local, teleseismic earthquakes or ambient noise, and other near-fault seismic observations, such as fault zone trapped waves (FZTWs), fault zone head waves (FZHWs), and P wave arrival delays from local and teleseismic earthquakes (e.g., Ben-Zion & Sammis, 2003; Yang, 2015; Yang et al., 2021; Jiang et al., 2021; She et al., 2022).

However, the definition of a fault damage zone is still under debate. The damage zone of an active fault is seismically recognized as a low-velocity zone (LVZ) with a reduction in seismic velocities and elastic moduli relative to the host rocks (Ben-Zion & Sammis, 2003). Other studies based primarily on geological mapping proposed further subdivisions of the fault core from the damage zone, such as the principal slip zone (Chester & Chester, 1998; Sibson, 1986, 2003), central and distal cores, and/or inner and outer damage zones (Perrin et al., 2016). Choi et al. (2016) summarized three main categories, i.e., along-fault, around-tip, and cross-fault, to define the damage zones, and in most cases, the boundary is determined as the distance where an abrupt decrease or fall off of the fracture frequency occurs.

The widths of fault damage zones estimated with geological and seismic methods are mostly around a few tens to hundreds of meters. For example, Riley et al. (2010) estimated the width of the damage zone of the Pajarito fault to be 80 m at Sawyer Canyon and 160-170 m at Bland and Frijoles Canyons in New Mexico. Based on fracture density field observations. Chester et al. (2005) inferred that the damage zone associated with the exhumed Punchbowl fault in the San Andreas fault (SAF) system in southern California is approximately 100 m. Li and Vernon (2001), and Qin et al. (2018) obtained a 70-100-m-wide damage zone along several strands of the San Jacinto Fault, based on the modeling of FZTWs. A 150-200 m width of fault damage zone was confirmed at this fault from local earthquake waveform modeling (Lewis et al. 2005; Yang & Zhu, 2010; Yang et al., 2014), and additional FZTW inversions (Share et al., 2019). Li et al. (2004) and Li (2021) inferred a low-velocity waveguide of ~150-200-m-wide at the Parkfield section of the SAF based on FZTWs. FZTWs recorded from dense seismic arrays indicate a ~200-m-wide rupture zone of the 2008 Wenchuan earthquake near the boundary of eastern Tibet and the Sichuan basin in Western China (Li et al., 2009) and a ~300-m-wide rupture zone of the 2001 Kunlun earthquake in the northern Tibetan Plateau (Li et al., 2005). Recently, Huang et al. (2020) obtained a width of ∼150–160 m low-velocity zone based on FZTWs at the Central section of the Longmen Shan fault that ruptured during the 2008 Wenchuan earthquake.

Other studies also reported a much wider damage zone. For example, a more than 1-km-wide damage zone of the Calico fault was first reported by InSAR (Fialko et al., 2002) and was later confirmed with detailed structure by FZTWs (Cochran et al., 2009) and travel times of local earthquakes (Yang et al., 2011). Based on relocated seismicity, Liu et al. (2003) observed that the aftershocks of the 1992 M7.3 Landers Earthquake occurred in a cloud that was wider than 1 km from the mainshock fault ruptures. Hauksson (2010) also found that most aftershocks in southern California occurred within ~2 km of the recent rupture zone, and background seismicity occurred at an even wider zone of ~10 km, which was interpreted as the seismic damage zone. Ma et al. (2019) found that the fault damage zone width showed great variability with the highest value in excess of 3 km inside the Tarim basin in Western China, even though most were in the range of 100–800 m along the strike-slip faults. In a similar region, a width of more than 2 km in carbonate rocks is inferred by well logs, cores, thin sections, and oil production (Wu et al., 2019). The width of the damage zone varies from ~50 to ~1000 m at the Arima–Takatsuki Tectonic Line and the Rokko–Awaji Fault Zone of southwest Japan (Lin & Yamashita, 2013). Based on the ambient noise tomography and teleseismic travel time anomaly, Qiu et al. (2021) observed 1- to 2-km-wide low-velocity zones with more intensely damaged inner zones along the rupture zone of the 2019 M7.1 Ridgecrest, California earthquake.

With a comparable length to the SAF, the Haiyuan fault is a major active left-lateral slip fault along the northeast edge of the Tibetan Plateau (Figure 1). Two large earthquakes occurred along or near the Haiyuan fault, the 1920 M~8 Haiyuan earthquake and the 1927 M8 Gulang earthquake, and the region between the two epicenters is named the “Tianzhu seismic gap” (Gaudemer et al., 1995). Shallow creep has been observed from geodetic data at the Laohushan section of the Haiyuan fault near the eastern end of the seismic gap (Jolivet et al., 2012, 2013; Li et al., 2021). Repeating earthquakes have also been detected in this creeping section from waveform cross-correlations of data from local seismic networks (Deng et al., 2020).

Compared with the multi-scale dense seismic network across and along the SAF and other recent rupture zones in California (e.g., Ben-Zion et al., 2015, Catchings et al., 2020), most of the recent seismological deployments in Northeastern Tibet (e.g., the ChinArray projects) focus on large-scale tomographic imaging and crustal deformation (e.g., Li et al., 2017; Wang et al., 2017; Shi et al., 2021; Tian et al., 2021), rather than high-resolution fault zone imaging with dense arrays across and along active faults. In addition, the relationship between the creep behavior and two large earthquakes along the Haiyuan fault, and the contribution of the creeping fault to future seismic hazards are still unclear.

In this study, we deploy dense nodal seismic stations across the creeping Laohushan section of the Haiyuan fault for high-resolution imaging of seismic structures based on local and teleseismic events. The internal structure of the fault damage zone can provide new insights to our understanding of the diverse fault slip behavior at intraplate regions and better ground motion predictions along and around active faults. In the next sections, we first describe the data and method, and then use waveforms generated by both local and teleseismic earthquakes to obtain fine structures of the damage zone of the fault section.

2. Data and method

2.1 Data

A 60-station dense array (three-component 5-Hz Smartsolo seismometers) is deployed at the Laohushan section of the Haiyuan fault from 2 July to 1 August 2020 (Figure 1). The 4-km long linear array, oriented ~15° clockwise from the north, is perpendicular to the local fault strike. The station spacing is the smallest (~6 m) near the fault trace, and gradually increases to ~500 m near both ends. In addition, we deploy a 2-D array around the study region with 50 seismic stations (three-component 5-s QS-05 seismometers) to help build a catalog of more local earthquakes with better hypocentral locations.

2.2 Delay time analysis

In addition to FZTWs from local earthquakes, travel time delays of body waves from local and teleseismic earthquakes provide an efficient way to determine fault zone boundaries (Li et al., 2007; Share et al., 2017; Yang et al., 2011; Yang et al., 2014). We largely follow the steps proposed by Yang et al. (2020) and Qiu et al. (2021) to process the teleseismic data. First, we obtain the first-arriving P phases from teleseismic earthquakes in USGS's NEIC earthquake catalog with magnitudes greater than Mw 4.5 (Figure 2). Then, 34 events (Table S2) with a good signal-to-noise ratio (SNR) are manually selected after band-pass filtering the waveform from 0.05 to 1.5 Hz (Yang et al., 2020). Second, we correct the topographic effects on the P wave's theoretical travel times using different near-surface velocities. Third, we use a 4-s-long window centered on the corrected P arrival to pick the arrival time of the P phase, based on the highest coefficient of the maximum or minimum peaks, to avoid possible errors associated with cycle-skipping or other artifacts. The travel time residuals between the picked arrival time and topography-corrected arrival time may reflect the local velocity variations in the crust assuming a flat Moho beneath the array. In addition, we compute waveform cross-correlations in a 4-s time window (2 s before and 2 s after picked arrivals) around the P waves between each station, to measure waveform similarity for stations inside and outside the fault zone.

Previous studies have shown that lithological contrasts across major faults often result in sharp bi-material interfaces, which may lead to significant differences in seismic radiation and rupture propagation (Ben-Zion & Sammis, 2003; Yang et al., 2015). FZHW propagating along bi-material fault interfaces from local earthquakes is an effective tool to estimate the velocity contrast of major fault interfaces (e.g., Ben-Zion & Malin, 1991; Zhao et al., 2010; McGuire & Ben-Zion, 2005; Lewis et al., 2007; Zhao & Peng, 2008). However, the accuracy of local earthquake location strongly affects the separation time between FZHWs and direct P waves and, thus, the resulting velocity contrast. As described in section 3, our local earthquake locations have large errors, mainly due to random timing errors in the seismic recordings of the 2D array (QS-05 seismometers). Hence, we only use teleseismic arrivals to image the velocity contrast in this region. Following the method of Ozakin et al. (2012), the travel time difference of a planar teleseismic wave with an incidence angle α recorded at two stations is given by

$$\Delta t_{North-South} = \frac{h}{V_{North}\cos(\alpha)} - \frac{h}{V_{South}\cos(\alpha)} \quad (1).$$

where h is the depth to which the velocity contrast extends, V_{South} and V_{North} indicate the average P wave velocity in crustal blocks south and north of the fault, respectively. The corresponding cross-fault velocity contrast can thus be written as

$$\frac{V_{North}}{V_{South}} = \frac{\mathrm{h}}{\mathrm{h}+\Delta t_{North-South}V_{South}\cos(\alpha)} \quad (2).$$

2.3 Catalog construction

Here we use EQTransformer (Mousavi et al., 2020), a method based on a deep neural network with an attention mechanism, to perform P and S wave detection and association for local earthquakes. We use threshold values of 0.3, 0.1, and 0.1 for detection, P-picking, and S-picking respectively, and a 5-s-long moving window and at least 10 stations for the phase association. Subsequently, we estimate absolute locations based on a 1D velocity model with a probabilistic nonlinear global-search algorithm called NonLinLoc (Lomax et al., 2000). The velocity model used in this study (Table S1) was constructed from nearby active and passive seismic investigations (Zhang et al., 2011; Deng et al., 2018). Next, we use the GrowClust (Trugman & Shearer, 2017) method to relocate all detected events, based on differential travel times estimated from cross-correlations of P and S waveforms within 2 s and 3 s window length, respectively.

2.4 Amplification and FZTW modeling

Low-velocity zones can produce relatively long-period high-amplitude seismic waves, and this amplification pattern may be a combined effect of lower elastic modulus, propagation (focusing and defocusing of body waves), and FZTWs (e.g., Li et al., 1990, 2000; Ben-Zion & Aki, 1990; Ben-Zion et al., 2003; Peng et al., 2003; Yang et al., 2020; Jiang et al., 2021; She et al., 2022; Song & Yang, 2022). To detect the low-velocity-zone related amplification of incoming waves, we calculate the normalized amplitude of the 3-Hz low-pass-filtered local events as the integral of the squared envelope of the waveforms within 20 s of the event origin time. We apply a 3-Hz lowpass filter because recent studies have shown that the dominant frequency of FZTWs is usually lower than 3 Hz (e.g., Wang et al., 2019; Qiu et al., 2020). In comparison, other body-wave phases such as P and S waves yield much higher peak frequencies and are often negligible at frequencies lower than 3 Hz when compared with FZTWs. Hence, the amplification pattern of the incoming seismic waves could be used to provide a first-order estimation of the width of the fault zone waveguide and detect candidate FZTWs for subsequent waveform modeling.

To model FZTWs, we use a genetic inversion algorithm that has been applied to FZTWs observed in previous studies (e.g., Ben-Zion et al., 2003; Lewis et al., 2005; Qiu et al., 2017) to invert the average fault zone waveguide.

The algorithm investigates a large number (e.g., 10,000) of simplified fault zone models, i.e., a rectangular low-velocity zone sandwiched by two quarter spaces with higher velocities (e.g., Fig. 5 of Ben-Zion et al. 2003), with different properties (e.g., width, attenuation, and velocity) through several (e.g., 50) iterations. Each model is evaluated by a fitness value, (1+CC)/2, where CC is the cross-correlation coefficient between the synthetic and observed waveforms. For a robust inversion process, the algorithm will converge to a group of models that fit the observation generally well (with a high fitness value) and share similar values of fault zone parameters in the last few iterations.

3. Results

3.1 P wave delay time analysis of teleseismic events

Figure 3 presents an example of the delay time analysis of an Mw5.5 teleseismic event (July 04, 2020, 01:34:45, Solomon Islands). We first compute the theoretical arrival times (blue dots) based on a global 1-D velocity model (IASP91, Kennett & Engdahl, 1991). Then, the topographic effect is further added to the theoretical arrival time pattern assuming a near-surface Vp of 3 km/s (red dots). The residuals between the observed (in green) and predicted (in red) arrival times illuminates the travel time delay associated with shallow materials beneath the array. Positive values at stations near the mapped fault surface trace (Figure 1) suggest a low-velocity zone beneath the surface trace.

To further verify this observation, we extend the delay time analysis to 34 teleseismic events (Table S2), and the mean and standard deviation of the residual arrival times are shown in Figure 4a. By choosing a threshold of 0.05 s (the average of the part of the array north to the fault surface trace), the fault zone width is approximately 1 km based on teleseismic P wave delay times. We note that, although near-surface Vp is often poorly constrained, it does not affect our estimation of the fault zone location and width as shown in Figure 4a, where the residual arrival times assuming different near-surface Vp (4 km/s, 3 km/s, and 2 km/s) are compared.

The similarity matrix, the cross correlation between every station pair, is shown in Figure 4b. As expected, the cross-correlation (CC) coefficient generally decreases with increasing distance (i.e., off-diagonal). However, in addition to the general trend, the similarity matrix can be further divided into three blocks with high CC coefficients near the diagonal line. These three groups of stations, with high similarity only between stations within the same group, likely correspond to significant variations in structures perpendicular to the fault (e.g., edges of low-velocity zones and cross-fault velocity contrast interface) that generate changes in waveforms recorded by stations in different groups.

In addition to the low-velocity zone, the delay time analysis also shows a ~0.15 s time difference between P wave arrival times recorded by stations at the two ends of the array (Figure 4a), indicating a lower P wave velocity in the crustal block north to the fault. Based on equation 2, the average velocity contrast across fault depends highly on the depth extent of the velocity contrast (H), the incidence angle of the incoming wave (alpha), and the mean Vp in the upper crust. Following previous studies, the Vp averaged in the crust is ~6.3 km/s (Zhang et al., 2011). Thus, in view of the average incident angle of 25° (Figure 2b), the minimum cross-fault velocity contrast is ~2%, as H should be smaller than the crustal thickness of 50 km (Deng et al., 2018; Shi et al., 2021). Alternatively, if we set H = 15 km (Sun et al., 2021), then Vp averaged over the top 15 km is ~6 km/s (Zhang et al., 2011), which yields a much larger cross-fault velocity contrast (~5%). Of course, if the velocity contrast is in a shallower depth, the value will be larger.

3.2 Local earthquake catalog

Based on EQTransformer phase detection, 28,303 P waves and 27,136 S waves are picked. After phase associations, we obtain 482 events. 14 QS stations have timing issues via checking the P-wave arrivals from 5 teleseismic events. The detailed information are shown in Figures S2-S6. Hence, we delete these stations for the following process. After removing the Root-Mean Squares (RMSs) larger than 1s during the absolute relocation process by NonLinLoc and merging the events within 6 s, we obtain 306 events. The time residual remains ~0.2 s, even for distances as large as 50 km. The horizontal errors are mostly smaller than 4 km, but the focal depths for most events are not well constrained, compared with the horizontal direction (Figure S1). A total of 117 events are relocated by Growclust based on the detected time sequences from EQtransformer and the cross-correlation between events, after removing the travel time input from 35 Smartsolo stations in the center of the linear array.

Figure 5 shows the final spatial distribution of local earthquakes. The QS-05 stations having timing issues are marked with green circles. As waveforms recorded by the Smartsolo stations are more stable and consistent than those of the QS-05 stations, the detected seismic phases associated with Smartsolo stations were five times more frequent than those associated with the QS-05 stations (Table S3). Hence, many of the relocated earthquakes (1/3 earthquakes) are constrained only by the linear Smartsolo array, resulting in a parallel direction with the array. Fortunately, the estimation of fault zone amplification from local events is not sensitive to their locations, which will be presented in section 3.3.

3.3 Amplification analysis

Figure 6 shows two examples of local events. The three-component waveforms indicate a clear arrival time delay and amplification of S waves near the zero offset. We further analyze the amplification pattern of local earthquakes by using the integral of the squared envelope of vertical component waveforms following Wang et al. (2019). Figure 7 shows such an amplitude pattern for four example events. Although the hypocentral distance varies from 3 to 30 km, the amplification is always the highest near the center of the array (i.e., fault surface trace), confirming that their locations do not strongly affect the peak location of the amplification pattern. In general, both the longest-duration and highest-amplitude S arrivals are observed near the fault surface trace, whereas the amplification decays with increasing fault-normal distance in both directions.

We further analyze the amplification pattern from earthquakes with a hypocentral distance of less than 35 km and a sufficiently high SNR. Observations of earthquakes at large distances recorded by fault zone arrays usually yield low SNR values (Peng et al., 2003) due to geometrical spreading and attenuation, and are not included in the analysis. The red curve in Figure 7 depicts the mean amplification pattern averaged over 62 local events (a detailed catalog is listed in Table S4) with error bars indicating the corresponding standard deviation. The average amplification pattern, consistent with those of a single event, also shows the highest amplitude near the fault surface trace. Based on a threshold determined by the largest value of sidelobes (dashed line in Fig. 7), a ~200-m-wide zone is outlined near the fault surface trace that significantly amplifies incoming seismic waves. We note that the fault zone width can vary depending on the choice of amplification threshold. To better constrain the fault zone width, we perform waveform modeling of FZTWs in the next section.

3.4 FZTW modeling

In addition to amplifying seismic waves, the ~200-m-wide low-velocity zone identified in section 3.3 can also act as a waveguide and generate FZTWs, if the damage zone is sufficiently uniform at depth. Following Qiu et al. (2021), we apply several preprocessing steps (e.g., Figure S6 of Qiu et al. 2017) to the S waveforms at fault parallel component (e.g., Figure S7) prior to FZTW analyses. These include removal of the instrument response and integration to displacement seismogram, a bandpass filter between 1-10 Hz (based on the SNR of the trapped wave signal), and conversion to the response of an equivalent SH line source by convolving the fault-parallel component S waveform with $1/\sqrt{t}$ (e.g., Igel et al., 2002, Vidale et al., 1985).

To detect FZTWs, we then visually inspect the recorded waveforms of local seismic events with a sufficient SNR of S wave. Four candidate events (red circles in Figure 5) are found to produce clear FZTWs at stations close to the fault surface trace (Figure S7). Compared to FZTWs identified from previous studies in California (e.g., Peng et al., 2003; Lewis & Ben-Zion, 2010; Qin et al., 2021; Qiu et al., 2021) and Turkey (e.g., Ben-Zion et al., 2003), signals observed in this study are much weaker (i.e., comparable to the amplitude of direct S wave) and yield relatively longer S-to-FZTW separation time (~1 s). Similar to Qiu et al. (2021), we first stack FZTWs of all four candidate events to enhance the signal quality prior to the waveform modeling. Figure 8 shows the stacking procedure: (1) S waveforms recorded by the station with the maximum amplitude of FZTW (red waveforms in Figure S7) are extracted from all four candidate events; (2) These waveforms are aligned according to the FZTW outlined by green solid lines and then stacked (black waveform); (3) The same amount of time shift obtained in step 2 is applied to recordings of other stations before stacking.

Figure 9a shows the resulting stacked S waveforms with the colored image highlighting the FZTW window. After stacking, direct S waves are significantly suppressed, while the FZTWs at stations with indexes between 30-33 are clearly preserved. We note that fault zone width inferred from FZTWs varies dramatically with frequency, i.e., from ~120 m at 1-3 Hz (Figure 9b) to ~60 m at 3-6 Hz (Figure 9c). This is likely due to a frequency dependent sensitivity of trapped waves to the complex geometry of the damage zone (Qiu et al., 2021). Specifically, the narrower fault zone width given by higher frequency FZTWs is consistent with a flower-shaped damage zone (i.e., width decreases with depth). This is because the fault zone at shallow depth often has a width that changes more rapidly with depth and thus may not be sufficiently uniform for waves at a higher frequency to generate constructive interference. Considering the clear fault zone width dispersion, we model the low and high frequency FZTWs separately to ensure better waveform fits, and the results are shown in Figures 10 and 11.

Following the modeling algorithm described in the method section, we run the inversion for 50 iterations with 200 models per iteration. The fault zone parameters in the last 10 generations (2,000 models) are shown in Figures 10b and 11b. We also compute the corresponding probability density functions using the frequency of each parameter value weighted by the fitness values (Ben-Zion et al., 2003). As expected, the best-fitting models from both low and high frequency FZTWs can generate synthetic seismograms that match with the observed FZHWs well (Figures 10 and 11). The width of the damage zone is ~140 m at 1-3 Hz frequency and ~50 m at 3-6 Hz. The estimated propagation distance inside the waveguide is ~5.4 km, which includes a propagation component along-strike (i.e., non-vertical incidence angle). If we assume that along-strike and vertical, distances are the same, it suggests a waveguide depth of ~4 km (= $5.4/\sqrt{2}$). The estimated average S wave velocity inside the fault zone and in the host rock is 0.9-1.7 km/s and ~3-4 km/s, respectively.

4. Discussion

4.1 Properties of Low-velocity zone and damage zone

From travel time delays of teleseismic P arrivals, we obtain an ~1-km-wide low-velocity zone. The teleseismic waves have almost identical paths before arriving at the near-zero offset stations. Hence, the delay time patterns are indicative of the shallow structure beneath those stations across the Haiyuan fault. This observation is consistent with field investigations from structural geology (Lin & Yamashita, 2013), as fractures in a broader damage fault zone could reduce seismic velocity and hence increase travel times for teleseismic waves. Based on teleseismic events, a low-velocity zone has also been found in other active faults, such as the San Jacinto fault zone (Share et al., 2017; Yang et al., 2014; Qin et al., 2021), rupture zones of the 1992 Landers earthquake (Li et al., 2007), and Calico fault zone (Yang et al., 2011) in Southern California.

Fault-zone amplifications of local events have been widely observed in both real fault zones (e.g., Eccles et al., 2015; Ellsworth & Malin, 2011; Li & Vernon, 2001; Li et al., 2000; Peng et al., 2003; Rovelli et al., 2002) and numerical simulations (e.g., Allam et al., 2015; Jahnke et al., 2002; Weng et al., 2016; Chen & Yang, 2020). From fault zone amplification of local events and waveform modeling of trapped waves, here we obtain a frequency dependent damage zone, which is ~ 150 m wide at 1-3 Hz and ~ 50 m at 3-6 Hz. We suggest that the 1-km-wide LVZ likely corresponds to a broader damage zone surrounding a flower-shaped inner zone with more intensive damages (Figure 12). Based on waveform modeling, the best-fitting fault zone Q value is ~10, and the fault zone S wave velocity is ~60% of that of the surrounding rocks. These results are similar to those presented in a recent study along the surface rupture of the 2019 Mw7.1 Ridgecrest earthquake (Qiu et al., 2021), which reported several 1- to 2-km-wide low-velocity zones with more intensely damaged inner zones (0.5-1.5 km wide) from FZTWs. In addition, the flower-like structure, with fracture connectivity increasing with depth is documented in rupture dynamic modeling (Okubo et al., 2019), and geological observations (Perrin et al., 2016).

Based on waveform modeling, we infer that the depth of the damage zone is ~4 km. This is in contrast to the deep fault damage zone extending to the bottom of the seismogenic zone as observed from FZTW studies (e.g., Li et al., 2000; Li & Vernon, 2001), but is more consistent with shallow damage zone interpretations based on FZHWs, P-wave delays and other observations (Ben-Zion et al., 2003; Li et al., 2007; Lewis & Ben-Zion, 2010; Qin et al., 2021; Peng et al., 2003; Yang et al. 2011, 2014; Yang & Zhu, 2010; Qiu et al., 2021). It is worth noting that the observed creep along the Laohushan section is also constrained in the top ~4 km of the Haiyuan Fault (Jolivet et al., 2012, 2013). In comparison, most repeating earthquakes in this region occur at depths of 5-10 km (Deng et al., 2020).

4.2 Creeping and non-creeping fault damage zone

The width of the damage zone at the creeping section of the Haiyuan fault is similar to that of well-studied fault damage zones, such as the San Jacinto Fault (Qin et al., 2021), and rupture zones of the 2019 Ridgecrest earthquake (Qiu et al., 2021) in southern California, likely indicating that the damage zone feature cannot distinguish creep and non-creeping faults. In fact, Li et al. (1997) deployed a dense array on the creeping section of the SAF near Cienega

Valley and the lock-to-creeping transition of the SAF near Parkfield, Central California. Based on waveform modeling of surface explosions, the Parkfield data are adequately fit by a shallow fault zone waveguide 170 m wide with an S velocity of 0.85 km/sec and an apparent Q of 30-40. At Cienega Valley in the creeping section, the fault zone waveguide appears to be approximately 120 m wide with an S velocity of 0.7 km/s and a Q-30. These results suggest that the seismic velocity reduction at the Parkfield section in the lock-to-creeping transition of the SAF is similar to that at Cienega Valley, where the SAF primarily creeps (Li et al., 2021).

The depth extent of the damage zone is ~4 km from the waveform modeling, which is consistent with the depth of shallow creep from geodetic observation in this region (Jolivet et al., 2012, 2013). This depth is also similar to other non-creeping faults, such as the San Jacinto fault (Lewis et al., 2005; Qin et al., 2021), the 2019 Ridgecrest earthquake rupture zone (Qiu et al., 2021), and the Parkfield segment of SAF (Lewis & Ben-Zion, 2010). Hence, we find no major structural difference between the creeping fault along the Haiyuan fault and the non-creeping faults in California. These studies, together with this study, suggest that the properties of low-velocity zones around active faults do not strongly depend on the fault slip behaviors (i.e., creep versus fast earthquake rupture). The mechanisms unrelated to dynamic brittle rupturing processes for the damage zone should be explored better. Alternatively, the creep behavior along the Laohushan section of the Haiyuan fault (and perhaps the creeping section of the SAF) could be a transient behavior (Chen et al., 2018), and infrequent large earthquakes can rupture through those apparent creeping sections (Deng et al., 2020), and result in permanent damages that can be detected by the seismic observations. Nevertheless, we need to investigate the fault damage zone properties along the sections that ruptured during the 1920 Haiyuan earthquake, to compare their similarities and differences with this study for a better understanding of the relationship between fault zone structure and fault behavior.

4.3 Velocity contrast of the bimaterial fault interface

The minimum velocity contrast along the Haiyuan fault is ~2%, which is comparable with the 1%~3% velocity contrast along the Garzê–Yushu Fault based on FZHW observations near the epicenter of the Mw 6.9 Yushu earthquake (Yang et al., 2015). An average contrast value of 5% would be estimated if the velocity contrast is limited to the upper 15 km of the crust (Sun et al., 2021). Similar velocity contrast of 5% to 10% is observed along the Parkfield section of the SAF (e.g., Ben-Zion & Malin, 1991; Zhao et al., 2010), the Calaveras Fault (e.g., Zhao & Peng, 2008), the Hayward Fault (e.g., Allam et al., 2014), and the North Anatolian Fault in Turkey (e.g., Bulut et al., 2012; Ozakin et al., 2012). From the joint inversion of receiver function and surface wave dispersion, Deng et al. (2018) also observed similar lower velocities in the northern block than that of the southern block, separated by the Haiyuan fault. Based on the observed velocity contrast, FZHWs propagating along the bi-material interface from local earthquakes is expected. However, the data quality, particularly for recordings near the fault, and the small number of local earthquakes near the fault limit our ability to detect the emergent FZHWs in this dataset. Longer-term high-quality broadband recordings may be needed for observing FZHWs in this region.

A bi-material fault interface is also expected to generate a preferred earthquake rupture direction if the initial stress is homogeneous (Ampuero & Ben-Zion, 2008; Weng et al., 2016), which is the slip direction of the slower block for a sub-shear rupture. For a super-shear rupture, the preferred direction is the slip direction of the faster block (e.g., Ben-Zion, 2001; Shi & Ben-Zion, 2006; Ampuero & Ben-Zion, 2008). With a left-lateral strike-slip motion, the preferred rupture direction for earthquakes with sub-shear rupture on the Haiyuan Fault would be to the west, while the direction with a super-shear rupture would be to the east. The surface rupture of the 1920 Haiyuan earthquake is approximately 240 km long (Zhang et al., 2005; Liu-Zeng et al., 2013) with a newly estimated moment magnitude of 7.9 (Ou et al., 2020). Although the epicenter is not well constrained, recent physics-based rupture modeling has suggested that an epicenter located further to the west side of the surface rupture would fit the observed shaking pattern better (Xu et al., 2019). If we assume that the velocity contrast observed in this section is the same as those in the rupture zone of the 1920 Haiyuan earthquake, then a southeast rupture propagation would be consistent with the Haiyuan mainshock being a super-shear rupture.

While we cannot confirm this directly with modern seismic recordings, it is worth noting several recent large strike-slip earthquakes occurring within the Tibetan plateau, such as the 2001 M7.9 Kunlun earthquake (Lin et al., 2002; Bouchon & Vallée, 2003), and the 2010 M6.9 Yushu earthquake (Wang & Mori, 2012) had super-shear ruptures and propagated predominately to the southeast. As mentioned before, Yang et al. (2015) found that the northern block across the Garze-Yushu fault has a slower seismic velocity than the southern block, consistent with the southeastern propagation of a super-shear rupture. It would be useful to examine whether similar velocity contrasts exist across the Kunlun fault, as well as surface ruptures of the 2021 M 7.4 Maduo, Qinghai, earthquake, where the rupture speed to the east of the mainshock epicenter appears to have reached super-shear (Yue et al., 2022; Li et al., 2022).

5. Conclusion

We deployed a dense temporary network of seismic stations at the creeping section of the Haiyuan fault in the northeastern Tibetan Plateau. Machine learning detection (EQTransformer), association, absolute relocation (NonLinLoc), and relative relocation (Growclust) are employed to obtain the local event catalog. Based on the local and teleseismic events, we found a broad ~1 km-wide low-velocity zone surrounding a flower-shaped inner damage zone, which is ~150 m in the shallower depth and reduces to ~50 m at larger depth. The depth extent of the damage zone in this region is ~4 km, similar to the depth extent of the shallow creep. We also found that the northern block of the fault has a lower velocity than the southern block. The velocity contrast is 2% if we consider the whole crust, and 5% if only the upper 15 km is considered. The damage zone of the creeping section of the Haiyuan fault does not appear to have a clear structural difference compared with non-creeping strike-slip faults elsewhere around the world. These observations are helpful for understanding diverse fault slip behavior and its contribution to ground motion and rupture propagation.

Data availability

The waveform data generated by teleseismic and local earthquakes used in this study are available at https://doi.org/10.6084/m9.figshare.19425977.

Acknowledgments

We thank Jianye Zong, Peng Zhang, Yan Wang, and Xiaoming Huang for participating in the field trip. We also appreciate Prof. Huajian Yao for providing part of the seismic instruments and Dr. Qiu Zhong for valuable suggestions on earthquake relocation. We thank two reviewers and the JGR editors for their valuable comments that have greatly improved the manuscript. This work was funded by the Natural Science Foundation of China (grant 42021002, 42104103), and the Youth Innovation Promotion Association CAS (YIPA2018035).

Reference:

Alam, M. K., Khan, F., Johnson, J., & Flicker, J. (2015). A comprehensive review of catastrophic faults in PV arrays: types, detection, and mitigation techniques. *IEEE Journal of Photovoltaics*, *5*(3), 982-997. https://doi.org/10.1109/JPHOTOV.2015.2397599

Ampuero, J. P., & Ben-Zion, Y. (2008), Cracks, pulses and macroscopic asymmetry of dynamic rupture on a bimaterial interface with velocity-weakening friction, Geophysical Journal International, 173(2), 674-692. https://doi.org/10.1111/j.1365-246X.2008.03736.x.

Ben-Zion, Y. (2001), Dynamic ruptures in recent models of earthquake faults, Journal of the Mechanics and Physics of Solids, 49(9), 2209-2244. https://doi.org/10.1016/S0022-5096(01)00036-9

Ben-Zion, Y., & Aki, K. (1990). Seismic radiation from an SH line source in a laterally heterogeneous planar fault zone. *Bulletin of the Seismological Society of America*, *80*(4), 971-994. https://doi.org/10.1785/BSSA0800040971

Ben-Zion, Y., & Malin, P. (1991), San Andreas Fault Zone Head Waves Near Parkfield, California, Science, 251(5001), 1592-1594, https://doi.org/10.1126/science.251.5001.1592.

Ben-Zion, Y., & Sammis, C. G. (2003), Characterization of Fault Zones, pure and applied geophysics, 160(3), 677-715. https://doi.org/10.1007/PL00012554

Ben-Zion, Y., Vernon, F. L., Ozakin, Y., Zigone, D., Ross, Z. E., Meng, H., White, M., Reyes, J., Hollis, D., & Barklage, M. (2015), Basic data features and results from a spatially dense seismic array on the San Jacinto fault zone, Geophysical Journal International, 202(1), 370-380, https://doi.org/doi:10.1093/gji/ggv142.

Ben-Zion, Y., Z. Peng, D. Okaya, L. Seeber, J. G. Armbruster, N. Ozer, A. J. Michael, S. Baris & M. Aktar (2003), A shallow fault zone structure illuminated by trapped waves in the Karadere-Düzce branch of the north Anatolian fault, western Turkey, Geophys. J. Int., 152, 699–717. https://doi.org/10.1046/j.1365-246X.2003.01870.x

Bouchon, M., & Vallée, M. (2003), Observation of Long Supershear Rupture During the Magnitude 8.1 Kunlunshan Earthquake, Science, 301(5634), 824-826. https://doi.org/10.1126/science.1086832.

Bulut, F., Ben-Zion, Y., & Bohnhoff, M. (2012). Evidence for a bimaterial interface along the Mudurnu segment of the North Anatolian Fault Zone from polarization analysis of P waves. *Earth and Planetary Science Letters*, *327*, 17-22. https://doi.org/10.1016/j.epsl.2012.02.001

Catchings, R. D., Goldman, M. R., Steidl, J. H., Chan, J. H., Allam, A. A., Criley, C. J., et al. (2020). Nodal seismograph recordings of the 2019 Ridgecrest earthquake sequence. Seismological Research Letters, 91, 3622–3633. https://doi.org/10.1785/0220200203

Chen, T., Liu-Zeng, J., Shao, Y. X., Zhang, P. Z., Oskin, M. E., Lei, Q. Y., & Li, Z. F. (2018). Geomorphic offsets along the creeping Laohu Shan section of the Haiyuan fault, northern Tibetan Plateau. Geosphere, 14(3), 1165-1186. https://doi.org/10.1130/GES01561.1

Chen, X., & Yang, H. (2020), Effects of seismogenic width and low-velocity zones on estimating slip-weakening distance from near-fault ground deformation, Geophysical Journal International, 223(3), 1497-1510. https://doi.org/10.1093/gji/ggaa385.

Chester, F. M., & Chester, J. S. (1998), Ultracataclasite structure and friction processes of the Punchbowl fault, San Andreas system, California, Tectonophysics, 295(1), 199-221. https://doi.org/10.1016/S0040-1951(98)00121-8.

Chester, F. M., Evans, J. P., & Biegel, R. L. (1993). Internal structure and weakening mechanisms of the San Andreas fault. *Journal of Geophysical Research: Solid Earth*, *98*(B1), 771-786. https://doi.org/10.1029/92JB01866

Chester, J. S., Chester, F. M., & Kronenberg, A. K. (2005), Fracture surface energy of the Punchbowl fault, San Andreas system, Nature, 437(7055), 133-136. https://doi.org/10.1038/nature03942.

Choi, J. H., Jin, K., Enkhbayar, D., Davvasambuu, B., Bayasgalan, A., & Kim, Y. S. (2012). Rupture propagation inferred from damage patterns, slip distribution, and segmentation of the 1957 MW8. 1 Gobi‐Altay earthquake rupture along the Bogd fault, Mongolia. *Journal of Geophysical Research: Solid Earth*, *117*(B12). https://doi.org/10.1029/2011JB008676

Choi, J. H., Edwards, P., Ko, K., & Kim, Y.S. (2016), Definition and classification of fault damage zones: A review and a new methodological approach, Earth-Science Reviews, 152, 70-87. https://doi.org/10.1016/j.earscirev.2015.11.006.

Cochran, E. S., Li, Y.-G., Shearer, P. M., Barbot, S., Fialko, Y., & Vidale, J. E. (2009), Seismic and geodetic evidence for extensive, long-lived fault damage zones, Geology, 37(4), 315-318. https://doi.org/10.1130/G25306A.1

Deng, Y., Li, J., Song, X., & Zhu, L. (2018). Joint Inversion for Lithospheric Structures: Implications for the Growth and Deformation in Northeastern Tibetan Plateau. Geophysical Research Letters, 45(9), 3951-3958. https://doi.org/10.1029/2018GL077486

Deng, Y., Peng, Z., & Liu-Zeng, J. (2020). Systematic search for repeating earthquakes along the Haiyuan fault system in Northeastern Tibet. Journal of Geophysical Research: Solid Earth, 125(7), e2020JB019583. https://doi.org/10.1029/2020JB019583

Eccles, J. D., Gulley, A. K., Malin, P. E., Boese, C. M., Townend, J., & Sutherland, R. (2015). Fault Zone Guided Wave generation on the locked, late interseismic Alpine fault, New Zealand. *Geophysical Research Letters*, *42*(14), 5736-5743. https://doi.org/10.1002/2015GL064208

Ellsworth, W. L., & Malin, P. E. (2011). Deep rock damage in the San Andreas Fault revealed by P-and S-type fault-zone-guided waves. *Geological Society, London, Special Publications*, *359*(1), 39-53. https://doi.org/10.1144/SP359.3

Fialko, Y., Sandwell, D., Agnew, D., Simons, M., Shearer, P., & Minster, B. (2002). Deformation on nearby faults induced by the 1999 Hector Mine earthquake. *Science*, *297*(5588), 1858-1862. https://doi.org/10.1126/science.107467

Gaudemer, Y., Tapponnier, P., Meyer, B., Peltzer, G., Shunmin, G., Zhitai, C., et al. (1995). Partitioning of crustal slip between linked, active faults in the eastern Qilian Shan, and evidence for a major seismic gap, the ‘Tianzhu gap’, on the western Haiyuan Fault, Gansu (China). Geophysical Journal International, 120(3), 599–645. https://doi.org/10.1111/j.1365-246X.1995.tb01842.x

Harris, R. A., & Day, S. M. (1997), Effects of a low-velocity zone on a dynamic rupture, Bulletin of the Seismological Society of America, 87(5), 1267-1280, https://doi.org/10.1785/BSSA0870051267.

Hauksson, E. (2010). Spatial separation of large earthquakes, aftershocks, and background seismicity: Analysis of interseismic and coseismic seismicity patterns in southern California. In *Seismogenesis and Earthquake Forecasting: The Frank Evison Volume II* (pp. 125-143). Springer, Basel. https://doi.org/10.1007/978-3-0346-0500-7_10

Huang, Y., Ampuero, J.-P., & Helmberger, D. V. (2014), Earthquake ruptures modulated by waves in damaged fault zones, J. Geophys. Res. Solid Earth, 119, 3133– 3154. https://doi.org/10.1002/2013JB010724.

Huang, Y., Li, H., Liu, X., Zhang, Y., Liu, M., Guan, Y., & Su, J. (2020), The Multiscale Structure of the Longmen Shan Central Fault Zone from Local and Teleseismic Data Recorded by Short‐Period Dense Arrays, Bulletin of the Seismological Society of America, 110(6), 3077-3087. https://doi.org/10.1785/0120190292.

Igel, H., Jahnke, G., & Ben-Zion, Y. (2002). Numerical simulation of fault zone guided waves: Accuracy and 3-D effects. Pure and Applied Geophysics, 159, 2067–2083. https://doi.org/10.1007/s00024-002-8724-9

Jahnke, G., Igel, H., & Ben-Zion, Y. (2002). Three-dimensional calculations of fault-zone-guided waves in various irregular structures. *Geophysical Journal International*, *151*(2), 416-426. https://doi.org/10.1046/j.1365-246X.2002.01784.x

Jiang, X., Hu, S., & Yang, H. (2021), Depth Extent and Vp/Vs Ratio of the Chenghai Fault Zone, Yunnan, China Constrained From Dense-Array-Based Teleseismic Receiver Functions, *Journal of Geophysical Research: Solid Earth*, *126*(8), e2021JB022190, https://doi.org/10.1029/2021JB022190.

Jolivet, R., Lasserre, C., Doin, M. P., Peltzer, G., Avouac, J. P., Sun, J., & Dailu, R. (2013). Spatio-temporal evolution of aseismic slip along the Haiyuan fault, China: Implications for fault frictional properties. Earth and Planetary Science Letters, 377-378, 23-33. https://doi.org/10.1016/j.epsl.2013.07.020

Kennett, B. L. N., & Engdahl, E. R. (1991). Traveltimes for global earthquake location and phase identification, Geophysical Journal International, 105(2), 429-465. https://doi.org/10.1111/j.1365-246X.1991.tb06724.x.

Kim, Y. S., & Sanderson, D. J. (2008). Earthquake and fault propagation, displacement and damage zones. *Structural geology: new research*, *1*, 99-117.

Kim, Y. S., & Sanderson, D. J. (2010). Inferred fluid flow through fault damage zones based on the observation of stalactites in carbonate caves. *Journal of Structural Geology*, *32*(9), 1305-1316. https://doi.org/10.1016/j.jsg.2009.04.017

Kim, Y.-S., Peacock, D. C. P., & Sanderson, D. J. (2004), Fault damage zones, Journal of Structural Geology, 26(3), 503-517. https://doi.org/10.1016/j.jsg.2003.08.002

Lewis, M. A., & Ben-Zion, Y. (2010). Diversity of fault zone damage and trapping structures in the Parkfield section of the San Andreas fault from comprehensive analysis of near fault seismograms. Geophysical Journal International, 183(3), 1579–1595. https://doi.org/10.1111/j.1365-246X.2010.04816.x

Lewis, M. A., Ben-Zion, Y., & McGuire, J. J. (2007). Imaging the deep structure of the San Andreas Fault south of Hollister with joint analysis of fault zone head and direct P arrivals. *Geophysical Journal International*, *169*(3), 1028-1042. https://doi.org/10.1111/j.1365-246X.2006.03319.x

Lewis, M. A., Peng, Z., Ben-Zion, Y., & Vernon, F. L. (2005), Shallow seismic trapping structure in the San Jacinto fault zone near Anza, California, Geophysical Journal International, 162(3), 867-881. https://doi.org/10.1111/j.1365-246X.2005.02684.x

Li, H., Zhu, L., & Yang, H. (2007). High-resolution structures of the Landers fault zone inferred from aftershock waveform data. Geophysical Journal International, 171(3), 1295–1307. https://doi.org/10.1111/j.1365-246X.2007.03608.x

Li, Q., Wan Y., Li C., Tang H., Tan K. & Wang D. (2022), Source Process Featuring Asymmetric Rupture Velocities of the 2021 Mw 7.4 Maduo, China, Earthquake from Teleseismic and Geodetic Data, Seismol. Res. Lett., https://doi.org/10.1785/0220210300.

Li, S. L., Zhang, X. K., & Fan, J. C. (2005). Study on rupture zone of the M= 8.1 Kunlun Mountain earthquake using fault-zone trapped waves. *Acta Seismologica Sinica*, *18*(1), 43-52. https://doi.org/10.1007/s11589-005-0005-0

Li, S., Lai, X., Yao, Z., & Yang, Q. (2009). Fault zone structures of northern and southern portions of the main central fault generated by the 2008 Wenchuan earthquake using fault zone trapped waves. *Earthquake Science*, *22*(4), 417-424. https://doi.org/10.1007/s11589-009-0417-3

Li, Y., & Vernon, F. L. (2001). Characterization of the San Jacinto fault zone near Anza, California, by fault zone trapped waves. Journal of Geophysical Research, 106(B12), 30,671–30,688. https://doi.org/10.1029/2000JB000107

Li, Y., Nocquet, J.-M., Shan, X., & Song, X. (2021). Geodetic observations of shallow creep on the Laohushan-Haiyuan fault, northeastern Tibet. Journal of Geophysical Research: Solid Earth, 126, e2020JB021576. https://doi.org/10.1029/2020JB021576

Li, Y., Vidale, J. E., Xu, F., & Aki, K. (2000), Depth-Dependent Structure of the Landers Fault Zone from Trapped Waves Generated by Aftershocks. Journal of Geophysical Research, 105(B3), 6237-6254. https://doi.org/10.1029/1999JB900449

Li, Y., Vidale, J., & Cochran, E. (2004). Low-velocity damaged structure of the San Andreas Fault at Parkfield from fault zone trapped waves. Geophysical Research Letters, 31, L12S06. https://doi.org/10.1029/2003GL019044

Li, Y., Wang, X., Zhang, R., Wu, Q., & Ding, Z. (2017), Crustal structure across the NE Tibetan Plateau and Ordos Block from the joint inversion of receiver functions and Rayleigh-wave dispersions, Tectonophysics, 705, 33-41. https://doi.org/10.1016/j.tecto.2017.03.020.

Li, Y.-G. (2021), Spatial-temporal characterization of the San Andreas Fault by fault-zone trapped waves at seismic experiment site, Parkfield, California, Earthquake Science, 34(3), 261-285. https://doi.org/10.29382/eqs-2021-0014.

Li, Y.-G., & Leary, P. C. (1990). Fault zone trapped seismic waves. *Bulletin of the Seismological Society of America*, *80*(5), 1245-1271. https://doi.org/10.1785/BSSA0800051245

Li, Y.-G., Ellsworth, W. L., Thurber, C. H., Malin, P. E., & Aki, K. (1997), Fault-zone guided waves from explosions in the San Andreas fault at Parkfield and Cienega Valley, California, Bulletin of the Seismological Society of America, 87(1), 210-221. https://doi.org/10.1785/BSSA0870010210.

Lin, A., & Yamashita, K. (2013). Spatial variations in damage zone width along strike-slip faults: An example from active faults in southwest Japan. Journal of Structural Geology, 57, 1-15. https://doi.org/10.1016/j.jsg.2013.10.006

Lin, A., Fu, B., Guo, J., Zeng, Q., Dang, G., He, W., & Zhao, Y. (2002), Co-Seismic Strike-Slip and Rupture Length Produced by the 2001 Ms 8.1 Central Kunlun Earthquake, Science, 296(5575), 2015-2017. https://doi.org/10.1126/science.1070879.

Liu, J., Sieh, K., & Hauksson, E. (2003), A Structural Interpretation of the Aftershock “Cloud” of the 1992 Mw 7.3 Landers Earthquake, Bulletin of the Seismological Society of America, 93(3), 1333-1344, doi:10.1785/0120020060.

Liu‐Zeng, J., Chen, T., Zhang, P. Z., Zhang, H. P., Zheng, W. J., Ren, Z. K., et al. (2013). Illuminating the active Haiyuan fault, China by airborne light detection and ranging. Chinese Science Bulletin, 58(1), 41–45. https://doi.org/10.1360/972012-1526

Lomax, A., Virieux, J., Volant, P., & Berge-Thierry, C. (2000). Probabilistic Earthquake Location in 3D and Layered Models. Advances in seismic event location (Vol. 18, pp. 101– 134).

Ma, D.-B., Wu, G.-H., Scarselli, N., Luo, X.-S., Han, J.-F., & Chen, Z.-Y. (2019). Seismic damage zone and width–throw scaling along the strike-slip faults in the Ordovician carbonates in the Tarim Basin. *Pet. Sci.* 16**,** 752–762. https://doi.org/10.1007/s12182-019-0352-4

Manighetti, I., King, G., & Sammis, C. G. (2004). The role of off-fault damage in the evolution of normal faults. *Earth and Planetary Science Letters*, *217*(3-4), 399-408. https://doi.org/10.1016/S0012-821X(03)00601-0

Manighetti, I., Zigone, D., Campillo, M., & Cotton, F. (2009). Self-similarity of the largest-scale segmentation of the faults: Implications for earthquake behavior. *Earth and Planetary Science Letters*, *288*(3-4), 370-381. https://doi.org/10.1016/j.epsl.2009.09.040

Marrett, R., & Allmendinger, R. W. (1992). Amount of extension on" small" faults: An example from the Viking graben. *Geology*, *20*(1), 47-50. https://doi.org/10.1130/0091-7613(1992)020<0047:AOEOSF>2.3.CO;2

McGuire, J., & Ben-Zion, Y. (2005). High-resolution imaging of the Bear Valley section of the San Andreas Fault at seismogenic depths with fault-zone head waves and relocated seismicity. *Geophysical Journal International*, *163*(1), 152-164. https://doi.org/10.1111/j.1365-246X.2005.02703.x

Mitchell, T. M., & Faulkner, D. R. (2009), The nature and origin of off-fault damage surrounding strike-slip fault zones with a wide range of displacements: A field study from the Atacama fault system, northern Chile, Journal of Structural Geology, 31(8), 802-816. https://doi.org/10.1016/j.jsg.2009.05.002

Mousavi, S. M., Ellsworth, W. L., Zhu, W., Chuang, L. Y., & Beroza, G. C. (2020). Earthquake transformer—an attentive deep-learning model for simultaneous earthquake detection and phase picking. *Nature communications*, *11*(1), 1-12. https://doi.org/10.1038/s41467-020-17591-w

Okubo, K., Bhat, H. S., Rougier, E., Marty, S., Schubnel, A., Lei, Z., Knight, E. E., & Klinger, Y. (2019), Dynamics, Radiation, and Overall Energy Budget of Earthquake Rupture With Coseismic Off-Fault Damage, Journal of Geophysical Research: Solid Earth, 124(11), 11771-11801, https://doi.org/10.1029/2019JB017304.

Ou, Q., Kulikova, G., Yu, J., Elliott, A., Parsons, B., & Walker, R. (2020), Magnitude of the 1920 Haiyuan Earthquake Reestimated Using Seismological and Geomorphological Methods, Journal of Geophysical Research: Solid Earth, 125(8), e2019JB019244, https://doi.org/10.1029/2019JB019244.

Ozakin, Y., Ben-Zion, Y., Aktar, M., Karabulut, H., & Peng, Z. (2012). Velocity contrast across the 1944 rupture zone of the North Anatolian fault east of Ismetpasa from analysis of teleseismic arrivals. Geophysical Research Letters, 39(8). https://doi.org/10.1029/2012GL051426

Peng, Z., & Deng, Y. (2022), Rapid Communications of Preliminary Results for the Recent Magnitude 6.6 Menyuan, Qinghai, China Earthquake Helps Scientists Better Study Intraplate Earthquakes, Earthquake Research Advances, 100119, https://doi.org/10.1016/j.eqrea.2022.100119.

Peng, Z., Ben - Zion, Y., Michael, A. J., & Zhu, L. (2003). Quantitative analysis of seismic fault zone waves in the rupture zone of the landers, 1992, California earthquake: Evidence for a shallow trapping structure. Geophysical Journal International, 155(3), 1021–1041. https://doi.org/10.1111/j.1365-246X.2003.02109.x

Perrin, C., Manighetti, I., Ampuero, J. P., Cappa, F., & Gaudemer, Y. (2016), Location of largest earthquake slip and fast rupture controlled by along-strike change in fault structural maturity due to fault growth, *Journal of Geophysical Research: Solid Earth*, *121*(5), 3666-3685. https://doi.org/10.1002/2015JB012671.

Qin, L., Ben-Zion, Y., Qiu, H., Share, P. E., Ross, Z. E., & Vernon, F. L. (2018), Internal structure of the San Jacinto fault zone in the trifurcation area southeast of Anza, California, from data of dense seismic arrays, Geophysical Journal International, 213(1), 98-114. https://doi.org/10.1093/gji/ggx540

Qin, L., Share, P. E., Qiu, H., Allam, A. A., Vernon, F. L., & Ben-Zion, Y. (2021). Internal structure of the San Jacinto fault zone at the Ramona Reservation, north of Anza, California, from dense array seismic data. Geophysical Journal International, 224(2), 1225-1241. https://doi.org/10.1093/gji/ggaa482

Qiu, H., Allam, A. A., Lin, F.C., & Ben-Zion, Y. (2020). Analysis of fault zone resonance modes recorded by a dense seismic array across the San Jacinto fault zone at Blackburn Saddle. Journal of Geophysical Research: Solid Earth, 125.

https://doi.org/10.1029/2020JB019756

Qiu, H., Ben-Zion, Y., Catchings, R., Goldman, M. R., Allam, A. A., & Steidl, J. (2021). Seismic imaging of the Mw 7.1 Ridgecrest earthquake rupture zone from data recorded by dense linear arrays. Journal of Geophysical Research: Solid Earth, 126, e2021JB022043. https://doi.org/10.1029/2021JB022043

Qiu, H., Ben-Zion, Y., Ross, Z. E., Share, P. E., & Vernon, F. L. (2017). Internal structure of the San Jacinto fault zone at Jackass Flat from data recorded by a dense linear array. Geophysical Journal International, 209(3), 1369–1388. https://doi.org/10.1093/gji/ggx096

Riley, P. R., Goodwin, L. B., & Lewis, C. J. (2010). Controls on fault damage zone width, structure, and symmetry in the Bandelier Tuff, New Mexico. *Journal of Structural Geology*, *32*(6), 766-780. https://doi.org/10.1016/j.jsg.2010.05.005

Rovelli, A., Caserta, A., Marra, F., & Ruggiero, V. (2002). Can seismic waves be trapped inside an inactive fault zone? The case study of Nocera Umbra, central Italy. *Bulletin of the Seismological Society of America*, *92*(6), 2217-2232. https://doi.org/10.1785/0120010288

Scholz, C. H., & Cowie, P. A. (1990). Determination of total strain from faulting using slip measurements. *Nature* 346, 837-839. https://doi.org/10.1038/346837a0

Schulz, S. E., & Evans, J. P. (1998). Spatial variability in microscopic deformation and composition of the Punchbowl fault, southern California: implications for mechanisms, fluid–rock interaction, and fault morphology. *Tectonophysics*, *295*(1-2), 223-244. https://doi.org/10.1016/S0040-1951(98)00122-X

Share, P. E., Allam, A. A., Ben-Zion, Y., Lin, F., &Vernon, F. L. (2019). Structural properties of the San Jancinto fault zone at Blackburn Saddle from seismic data of a dense linear array. Pure and Applied Geophysics, 176(3), 1169–1191. https://doi.org/10.1007/s00024-018-1988-5

Share, P. E., Ben-Zion, Y., Ross, Z. E., Qiu, H., & Vernon, F. (2017). Internal structure of the San Jacinto fault zone at Blackburn Saddle from seismic data of a linear array. Geophysical Journal International, 210(2), 819–832. https://doi.org/10.1093/gji/ggx191

She, Y., Yao, H., Yang, H., Wang, J., & Feng, J. (2022), Constraining the depth extent of low-velocity zone along the Chenghai Fault by dense array ambient noise interferometry and horizontal-to-vertical spectral ratio, Tectonophysics, 827, 229265. https://doi.org/10.1016/j.tecto.2022.229265

Shi, Y., Gao, Y., & Lu, L. (2021), Receiver Function Structures Beneath the Haiyuan Fault on the Northeastern Margin of the Tibetan Plateau, Earthquake Science, 34(4), 367-377. https://doi.org/10.29382/eqs-2021-0055.

Shi, Z., & Ben-Zion, Y. (2006), Dynamic rupture on a bimaterial interface governed by slip-weakening friction, Geophysical Journal International, 165(2), 469-484. https://doi.org/10.1111/j.1365-246X.2006.02853.x.

Sibson, R. H. (1986). Earthquakes and rock deformation in crustal fault zones. *Annual Review of Earth and Planetary Sciences*, *14*, 149. https://doi.org/10.1146/annurev.ea.14.050186.001053

Sibson, R. H. (2003). Thickness of the seismic slip zone. *Bulletin of the Seismological Society of America*, *93*(3), 1169-1178. https://doi.org/10.1785/0120020061

Song, J., & Yang, H. (2022). Seismic site response inferred from records at a dense linear array across the Chenghai fault zone, Binchuan, Yunnan. Journal of Geophysical Research: Solid Earth, 127, e2021JB022710. https://doi.org/10.1029/2021JB022710

Sun, Q., Pei, S., Cui, Z., Chen, Y. J., Liu, Y., Xue, X., Li, J., Li, L., & Zuo, H. (2021), Structure-controlled asperities of the 1920 Haiyuan M8.5 and 1927 Gulang M8 earthquakes, NE Tibet, China, revealed by high-resolution seismic tomography, Scientific Reports, 11(1), 5090, https://doi.org/10.1038/s41598-021-84642-7.

Tian, X., Bai, Z., Klemperer, S. L., Liang, X., Liu, Z., Wang, X., Yang, X., Wei, Y., & Zhu, G. (2021), Crustal-scale wedge tectonics at the narrow boundary between the Tibetan Plateau and Ordos block, Earth and Planetary Science Letters, 554, 116700. https://doi.org/10.1016/j.epsl.2020.116700.

Torabi, A., Ellingsen, T. S. S., Johannessen, M. U., Alaei, B., Rotevatn, A., & Chiarella, D. (2020), Fault zone architecture and its scaling laws: where does the damage zone start and stop?, Geological Society, London, Special Publications, 496(1), 99, https://doi.org/10.1144/SP496-2018-151.

Trugman, D. T., & Shearer, P. M. (2017). GrowClust: A hierarchical clustering algorithm for relative earthquake relocation, with application to the Spanish Springs and Sheldon, Nevada, earthquake sequences. Seismological Research Letters, 88(2A), 379–391. https://doi.org/10.1785/0220160188

Vidale, J., Helmberger, D. V., & Clayton, R. W. (1985). Finite-difference seismograms for SH waves. Bulletin of the Seismological Society of America, 75(6), 1765–1782. https://doi.org/10.1785/BSSA0750061765

Walsh, J. J., & Watterson, J. (1991). Geometric and kinematic coherence and scale effects in normal fault systems. *Geological Society, London, Special Publications*, *56*(1), 193-203. https://doi.org/10.1144/GSL.SP.1991.056.01.13

Wang, D., & Mori, J. (2012), The 2010 Qinghai, China, Earthquake: A Moderate Earthquake with Supershear Rupture, Bulletin of the Seismological Society of America, 102(1), 301-308. https://doi.org/10.1785/0120110034.

Wang, W., Wu, J., Fang, L., Lai, G., & Cai, Y. (2017), Sedimentary and crustal thicknesses and Poisson's ratios for the NE Tibetan Plateau and its adjacent regions based on dense seismic arrays, Earth & Planetary Science Letters, 462, 76-85. https://doi.org/10.1016/j.epsl.2016.12.040.

Wang, Y., Allam, A., & Lin, F.‐C. (2019). Imaging the Fault Damage Zone of the San Jacinto Fault Near Anza With Ambient Noise Tomography Using a Dense Nodal Array. Geophysical Research Letters, 46. https://doi.org/10.1029/2019GL084835

Weng, H., Yang, H., Zhang, Z., & Chen, X. (2016), Earthquake rupture extents and coseismic slips promoted by damaged fault zones, *Journal of Geophysical Research: Solid Earth*, *121*(6), 4446-4457. https://doi.org/10.1002/2015JB012713.

Wilson, J. E., Chester, J. S., & Chester, F. M. (2003). Microfracture analysis of fault growth and wear processes, Punchbowl Fault, San Andreas system, California. *Journal of Structural Geology*, *25*(11), 1855-1873. https://doi.org/10.1016/S0191-8141(03)00036-1

Wu, G., Gao, L., Zhang, Y., Ning, C., & Xie, E. (2019). Fracture attributes in reservoir-scale carbonate fault damage zones and implications for damage zone width and growth in the deep subsurface. *Journal of Structural Geology*, *118*, 181-193. https://doi.org/10.1016/j.jsg.2018.10.008

Xu, X., Zhang, Z., Hu, F., & Chen, X. (2019). Dynamic Rupture Simulations of the 1920 Ms 8.5 Haiyuan Earthquake in China. Bulletin of the Seismological Society of America, 109(5), 2009-2020. https://doi.org/10.1785/0120190061

Yang, H. (2015). Recent advances in imaging crustal fault zones: A review. Earthquake Science, 28(2), 151–162. https://doi.org/10.1007/s11589-015-0114-3

Yang, H., & Zhu, L. (2010). Shallow low‐velocity zone of the San Jacinto fault from local earthquake waveform modeling. Geophysical Journal International, 183(1), 421–432. https://doi.org/10.1111/j.1365-246X.2010.04744.x

Yang, H., Duan, Y., Song, J., Jiang, X., Tian, X., Yang, W., et al. (2020). Fine structure of the Chenghai fault zone, Yunnan, China, constrained from teleseismic travel time and ambient noise tomography. Journal of Geophysical Research: Solid Earth, 125, e2020JB019565. https://doi.org/10.1029/2020JB019565

Yang, H., Duan, Y., Song, J., Wang, W., Yang, W., Tian, X., & Wang, B. (2021), Illuminating high-resolution crustal fault zones using multi-scale dense arrays and airgun source, Earthquake Research Advances, 1(1), 100001. https://doi.org/10.1016/j.eqrea.2021.100001.

Yang, H., Li, Z., Peng, Z., Ben‐Zion, Y., & Vernon, F. (2014). Low velocity zones along the San Jacinto Fault, Southern California, from body waves recorded in dense linear arrays. Journal of Geophysical Research: Solid Earth, 119, 8976-8990. https://doi.org/10.1002/2014JB011548

Yang, H., Zhu, L., & Cochran, E. S. (2011). Seismic structures of the calico fault zone inferred from local earthquake travel time modelling. Geophysical Journal International, 186(2), 760–770. https://doi.org/10.1111/j.1365-246X.2011.05055.x

Yang, W., Peng, Z., Wang, B., Li, Z., & Yuan, S. (2015). Velocity contrast along the rupture zone of the 2010 Mw6.9 Yushu, China, earthquake from fault zone head waves. Earth and Planetary Science Letters, 416, 91-97. https://doi.org/10.1016/j.epsl.2015.01.043

Yue, H., Shen, Z.K., Zhao, Z., Wang T., Cao B., Li Z., et al. (2022), Rupture process of the 2021 M7.4 Maduo earthquake and implication for deformation mode of the Songpan-Ganzi terrane in Tibetan Plateau, Proc. Natl. Acad. Sci.,119(23), e2116445119. https://doi.org10.1073/pnas.2116445119.

Zhang, P., Min, W., Deng, Q., & Mao, F. (2005), Paleoearthquake rupture behavior and recurrence of great earthquakes along the Haiyuan fault, northwestern China, Science in China Series D: Earth Sciences, 48(3), 364-375. http://dx.doi.org/10.1360/02yd0464.

Zhang, Z., Klemperer, S., Bai, Z., Chen, Y., & Teng, J. (2011). Crustal structure of the Paleozoic Kunlun orogeny from an active-source seismic profile between Moba and Guide in East Tibet, China. Gondwana Research, 19(4), 994-1007. http://dx.doi.org/10.1016/j.gr.2010.09.008

Zhao, P., & Peng, Z. (2008). Velocity contrast along the Calaveras fault from analysis of fault zone head waves generated by repeating earthquakes. Geophys. Res. Lett. 35(1), L01303. https://doi.org/10.1029/2007GL031810

Zhao, P., Peng, Z., Shi, Z., Lewis, M. A., & Ben-Zion, Y. (2010), Variations of the velocity contrast and rupture properties of M6 earthquakes along the Parkfield section of the San Andreas fault, Geophysical Journal International, 180(2), 765-780, https://doi.org/10.1111/j.1365-246X.2009.04436.x.

Figure Caption

Figure 1. Map overview of the deployed stations. (a) Configurations of the linear (red circles) and 2-D (red triangles) arrays at the Laohushan section of the Haiyuan fault. Fault surface trace is mapped from the airborne LiDAR (Liu-Zeng et al., 2013). The blue rectangle outlines the region with possible creep (Jolivet et al., 2012, 2013). The insert map shows a larger region of the Tibetan Plateau. The red rectangle marks the study region for (a). HYF: Haiyuan fault; KF: Kunlun fault; XHF: Xianshuihe fault; ATF: Altyn Tagh fault. (b) A zoom-in map of the linear fault zone array (the dotted region in (a)).

Figure 2. The information of teleseismic events in this study. (a) Distribution of teleseismic events analyzed in this study. (b) The theoretical incident angle distribution of the

analyzed events. There are more than 100 teleseismic events with Mw>4.5 during the deployed time. After visual inspection, we only include 34 events with high SNR in the teleseismic delay time analysis.

Figure 3. P wave delay time analysis of an example teleseismic event (Earthquake UTC time: 2020-07-04 01:34:45 Mw5.5, Solomon Islands). (a) Arrival times of the theoretical, topo-corrected (assuming a near-surface Vp of 3 km/s), and observed P waves are shown in blue, red, and green respectively; (b) The residuals between arrival times in green and red, with the reference station at the center of the fault; (c) The topography along this array.

Figure 4. (a) The mean and standard deviation of residual arrival time pattern for P waves over 34 teleseismic events, with the reference station at the center of the fault. Different color indicates different near-surface Vp used in topographic correction. The low-velocity zone indicates a ~1-km-wide fault damage zone. (b) The similarity matrix averaged over 34 teleseismic events. Each pixel illustrates the maximum cross correlation coefficient between P waves recorded by a pair of stations averaged over all analyzed teleseismic events. Three blocks are outlined with dotted boxes. The red vertical bar denotes the 1 km low-velocity zone identified in (a).

Figure 5. Local events distribution during the one month of July 2020 after relocated by NonLinLoc and Growclust. The arrows marked the locations for local events in Figure 6. Red circles outlined the events having clear trapped waves in Figure S7.

Figure 6. Two examples of three-component raw seismograms generated by two local events (Earthquake UTC time: 2020-07-23 14:53:09 (top), 2020-07-15 22:39:39 (bottom)). The rough arrival times of P and S wave are labeled. Locations of these events are marked with arrows in Figure 5. The red bar on the right denotes the low-velocity zone identified from the analysis of the fault zone amplification pattern in Figure 7 (shaded area).

Figure 7. The mean and standard deviations of amplification patterns of 62 local events using the vertical component. Amplification patterns for four example events with a wide range of hypocentral distances are also shown. A ~200-m-wide high amplification zone (i.e., the mean amplification higher than the dashed line) is highlighted in the center of the fault.

Figure 8. Nearly identical candidate FZTWs, outlined by green vertical lines observed in

the example station ST33 near fault for all four candidate events. The top black trace is the linear stack of waveforms from four candidate events after aligning them in the FZTW window. 0 s in the x-axis denotes the start of the FZTW window.

Figure 9. (a) Stacked waveforms of all candidate FZTWs. Colors represent the wavefield within the FZTW window, whereas the red dashed curve denotes the maximum amplitude within the FZTW window. (b) Same as (a) for Candidate FZTWs bandpass filtered at 1-3 Hz. The maximum amplitude pattern (red dashed curve) suggests a ~120-m wide damage zone. (c) Same as (b) for FZTWs bandpass filtered at 3-6 Hz. A narrower (~60-m) fault damage zone can be inferred.

Figure 10. Inversion results for FZTWs filtered at 1-3 Hz and observed between stations 27–35, averaged over all four candidates shown in Fig. 8. Top panel: Comparison between synthetic waveforms (blue) computed using the best-fitting model parameters (black stars in (b)) and the observed FZTWs (in black). Bottom panels: Fitness values of fault-zone model parameters from the last 10 generations of the inversion (green dots). The best-fitting parameters (black stars) are displayed in each panel and used to generate the synthetic waveforms shown in (a). The red bar outlines stations with clear FZTWs. The black curve indicates the probability density function of model parameters shown as green dots.

Figure 11. Same as Figure 10 for waveform modeling of FZTWs filtered at 3-6 Hz. Consistent parameters are obtained from modeling of both high and low frequency FZTWs. The good waveform fits, combined with the consistency between best fitting parameters and peaks of the probability density functions, suggest that the best-fitting model parameters provide robust estimates of the average properties of the fault-zone waveguide.

Figure 12 (a) Schematic diagram of fault damage zone inferred from the teleseismic and local events. A 1 km low-velocity zone is outlined for the entire damage zone, and the damage inner zone has the flower-shaped feature, i.e., width decreases with depth. The south side of the fault has a faster velocity than the north side based on the teleseismic events. The center part of the array is magnified in the lower panel. (b) A zoom-in google map showing the array geometry, active fault trace, and topography in the study region. Stations used in the waveform modeling of FZTWs at 3-6 Hz (Fig. 11) are shown in red, whereas stations in both red and blue are included in the modeling of FZTWs at 1-3 Hz (Fig. 10). (c) A cross-section schematic diagram showing the flower-type trapping structure.

Figure1.

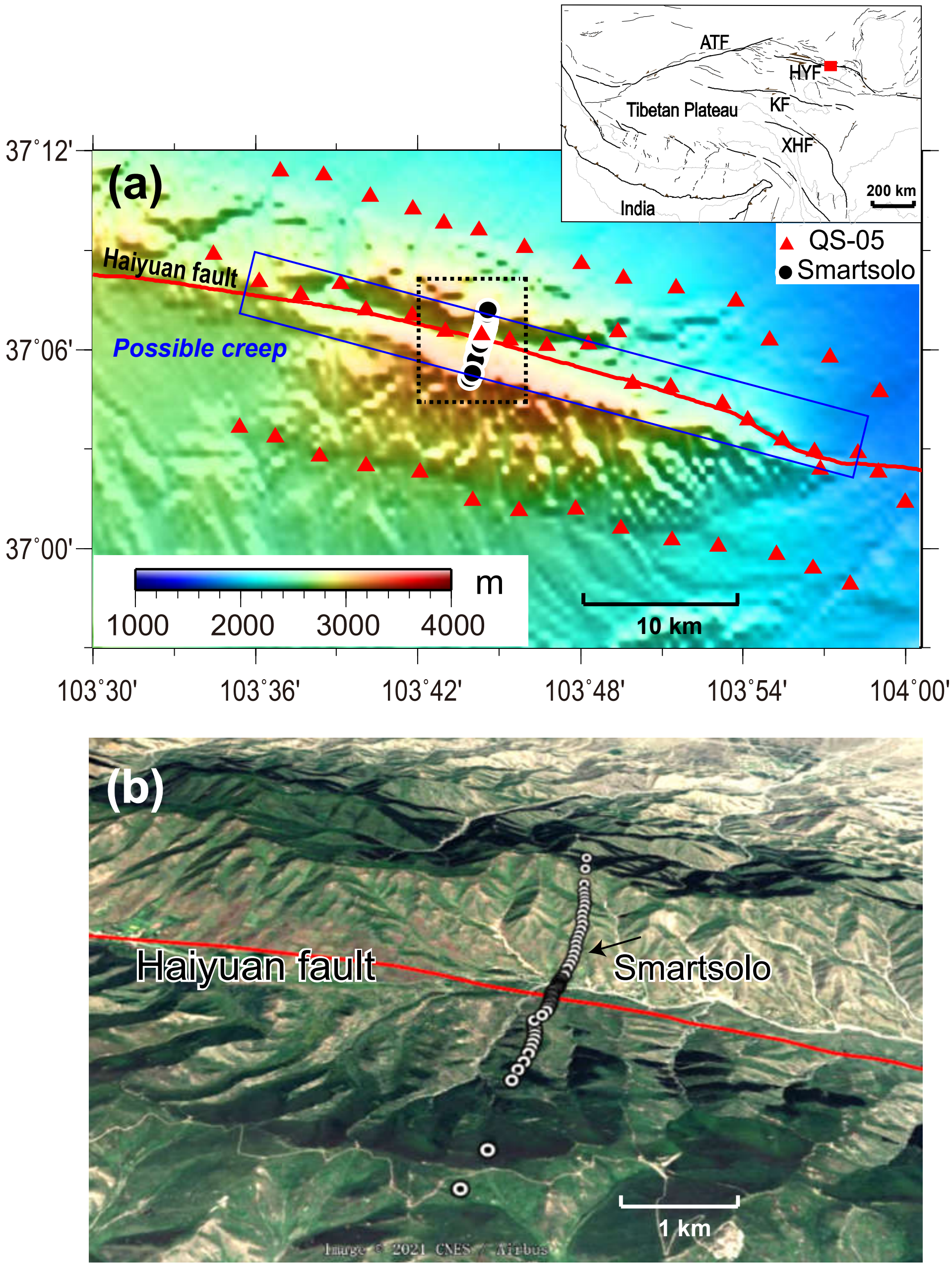

ATF
HYF
Tibetan Plateau
KF
XHF
India
200 km
37°12'
37°06'
37°00'
(a)
Haiyuan fault
Possible creep
QS-05
Smartsolo
m
1000
2000
3000
4000
10 km
103°30'
103°36'
103°42'
103°48'
103°54'
104°00'
(b)
Haiyuan fault
Smartsolo
1 km
Image © 2021 CNES / Airbus

Figure2.

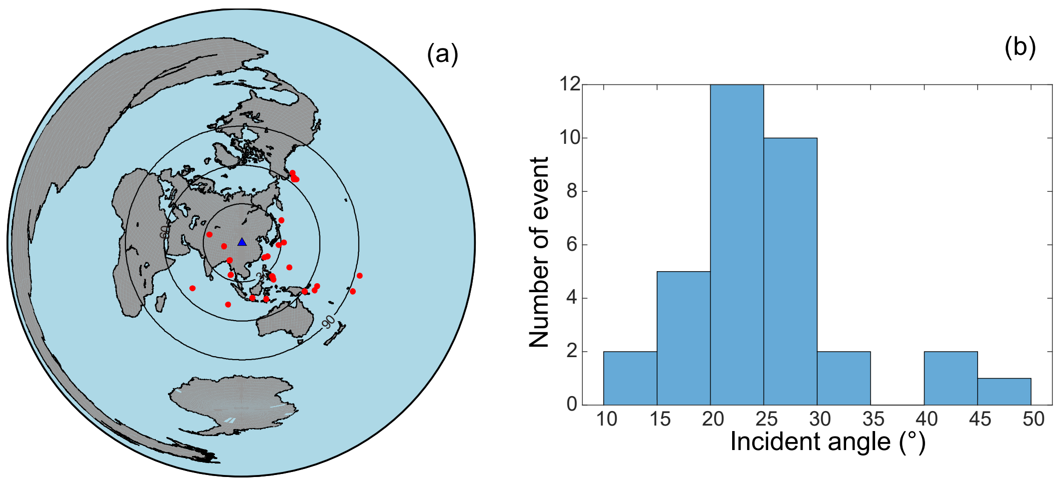
(a)
90
(b)
Number of event
Incident angle (°)
0
2
4
6
8
10
12
10
15
20
25
30
35
40
45
50

Figure3.

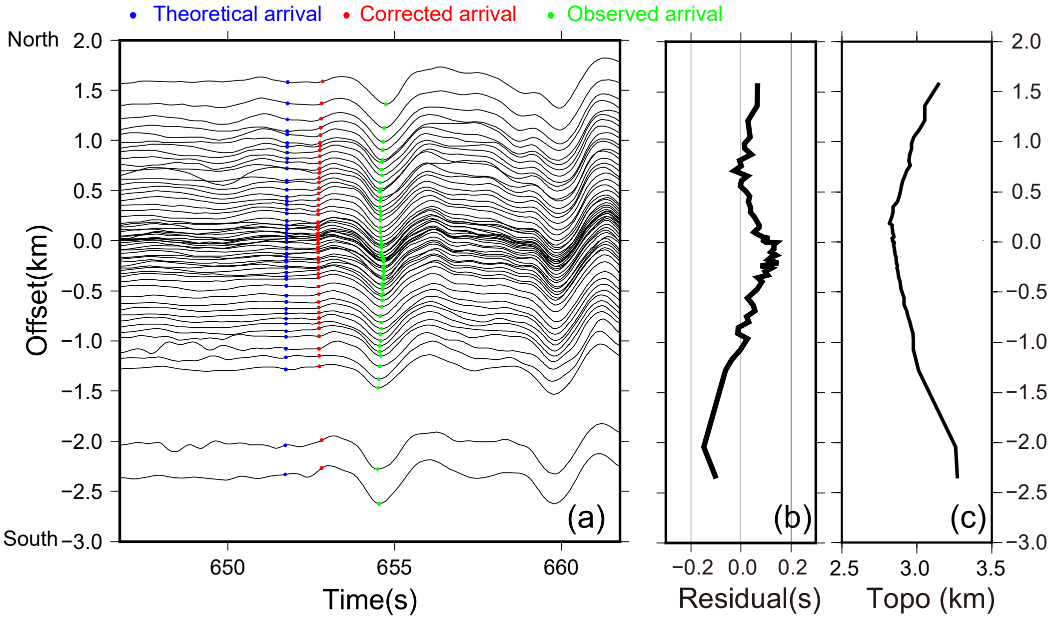

Theoretical arrival
Corrected arrival
Observed arrival
North
South
2.0
1.5
1.0
0.5
0.0
−0.5
−1.0
−1.5
−2.0
−2.5
−3.0
Offset(km)
650
655
660
Time(s)
(a)
−0.2
0.0
0.2
Residual(s)
(b)
2.5
3.0
3.5
Topo (km)
(c)

Figure4.

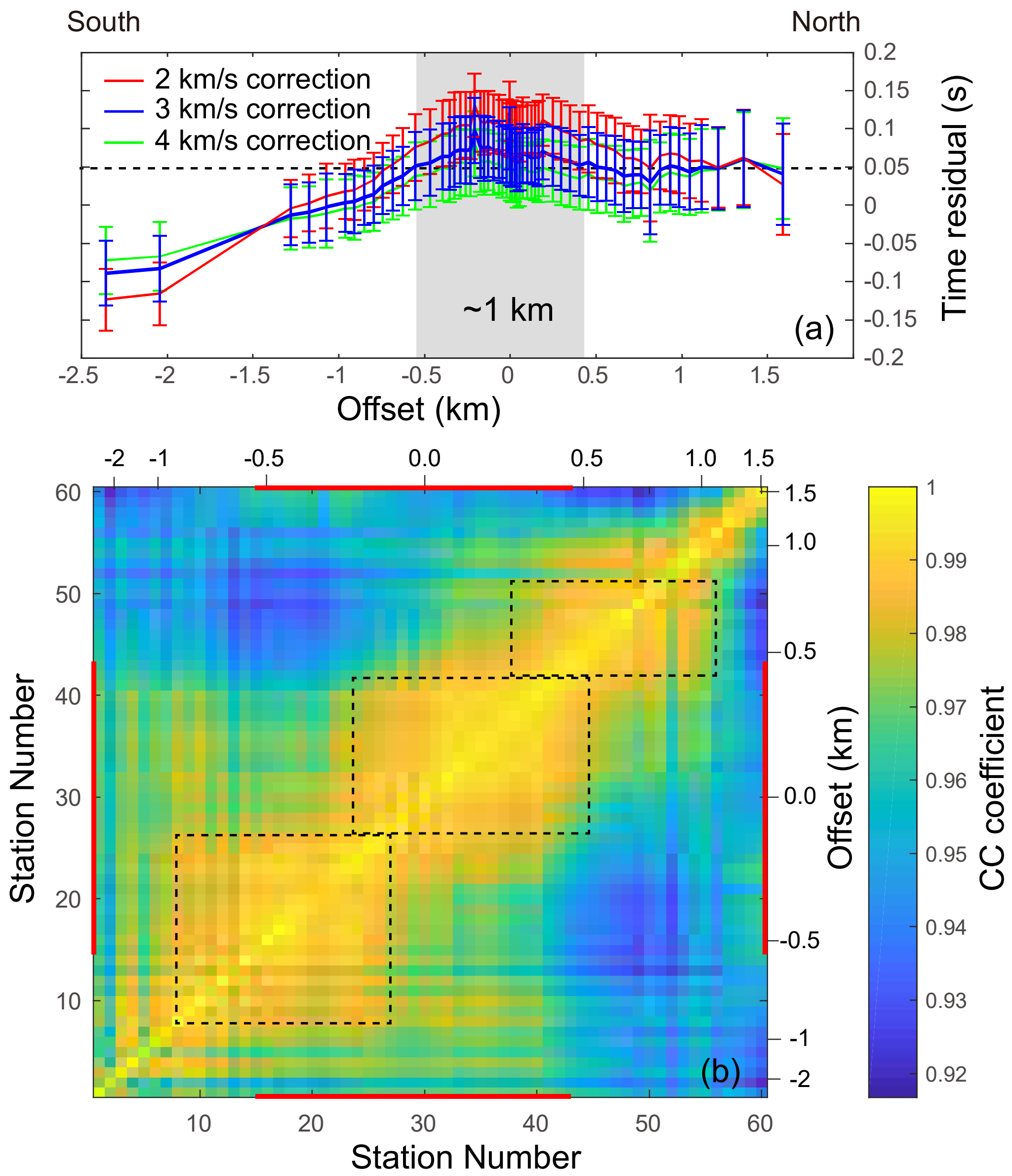
South
North
2 km/s correction
3 km/s correction
4 km/s correction
~1 km
(a)
Time residual (s)
Offset (km)
Station Number
Offset (km)
CC coefficient
(b)
Station Number

Figure5.

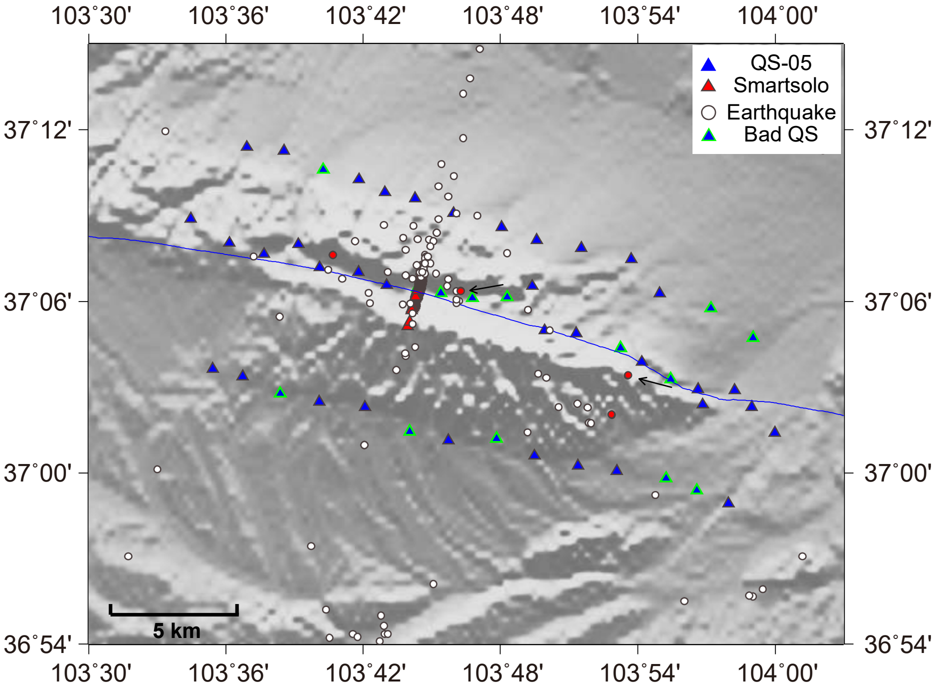

103°30'
103°36'
103°42'
103°48'
103°54'
104°00'
37°12'
37°06'
37°00'
36°54'
QS-05
Smartsolo
Earthquake
Bad QS
5 km

Figure6.

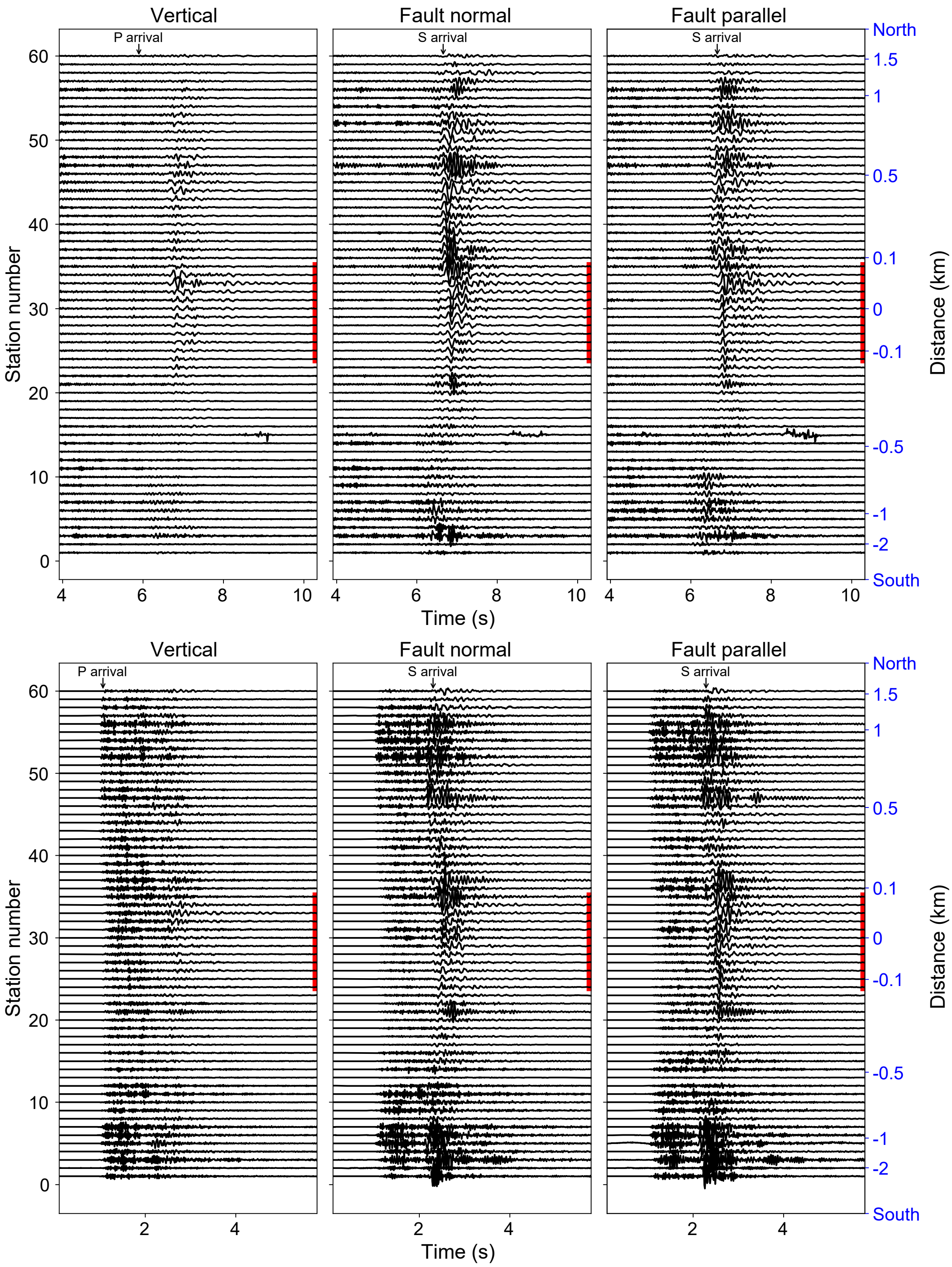
Vertical
Fault normal
Fault parallel
P arrival
S arrival
S arrival
North
South
Station number
Distance (km)
Time (s)
60
50
40
30
20
10
0
4
6
8
10
1.5
1
0.5
0.1
0
-0.1
-0.5
-1
-2
Vertical
Fault normal
Fault parallel
P arrival
S arrival
S arrival
North
South
Station number
Distance (km)
Time (s)
2
4

Figure7.

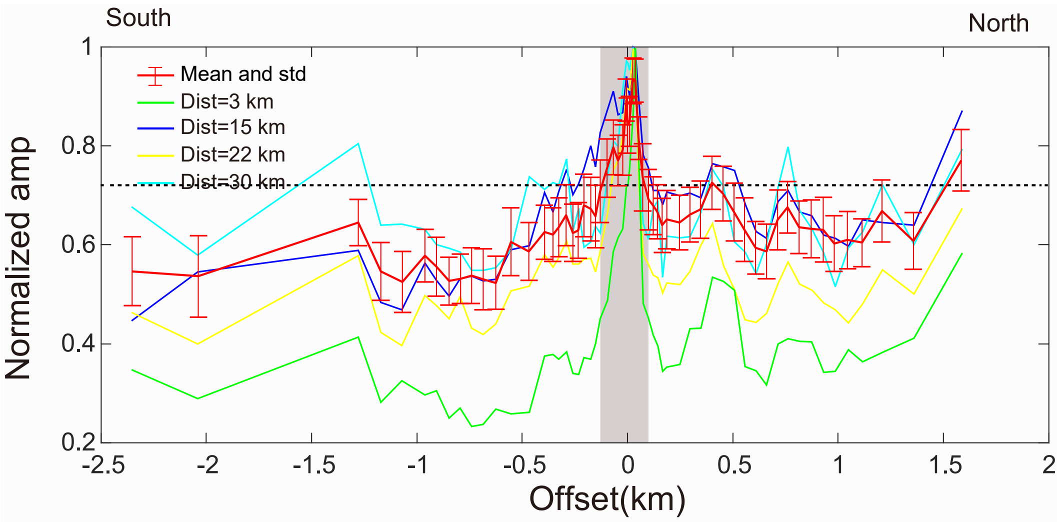

South
North
Normalized amp
Mean and std
Dist=3 km
Dist=15 km
Dist=22 km
Dist=30 km
Offset(km)
1
0.8
0.6
0.4
0.2
-2.5
-2
-1.5
-1
-0.5
0
0.5
1
1.5
2

Figure8.

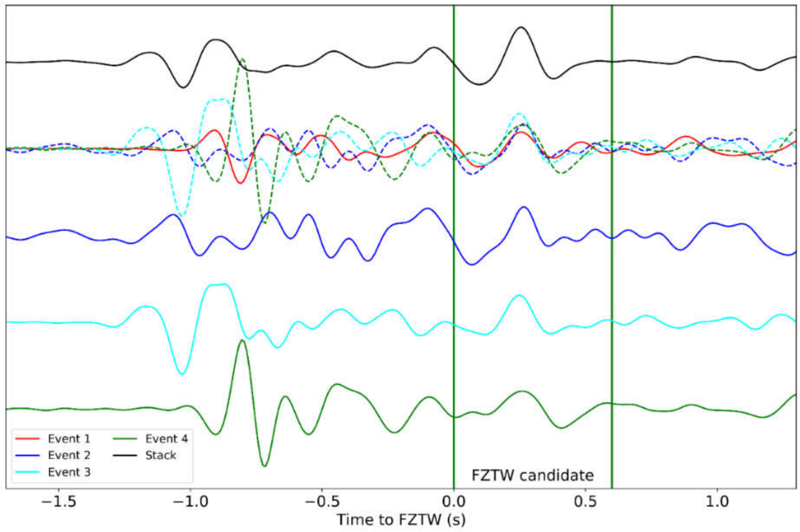

Event 1
Event 2
Event 3
Event 4
Stack
FZTW candidate
−1.5
−1.0
−0.5
0.0
0.5
1.0
Time to FZTW (s)

Figure9.

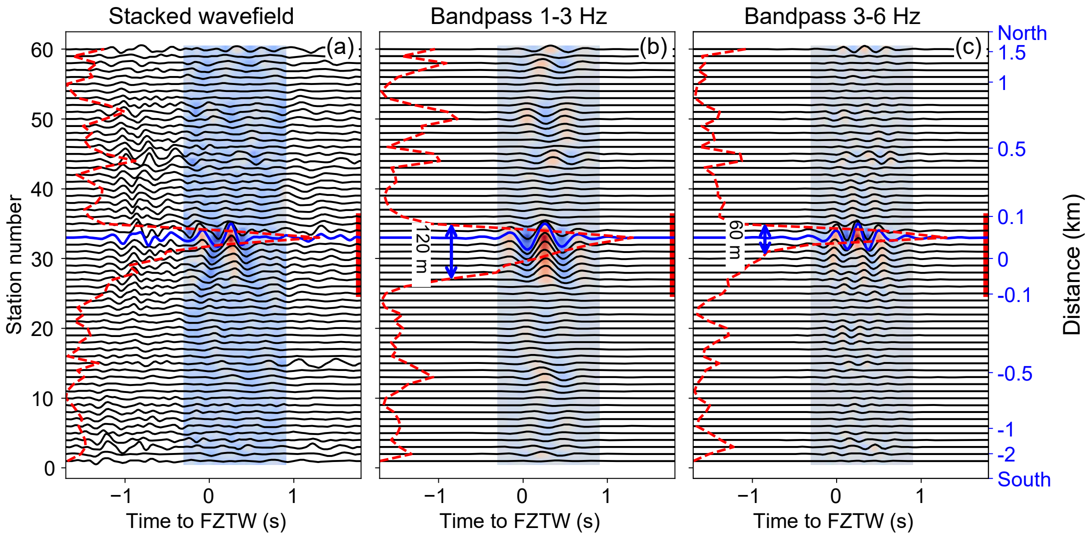

Stacked wavefield
Bandpass 1-3 Hz
Bandpass 3-6 Hz
(a)
(b)
(c)
Station number
Time to FZTW (s)
Distance (km)
North
South
120 m
60 m

Figure10.

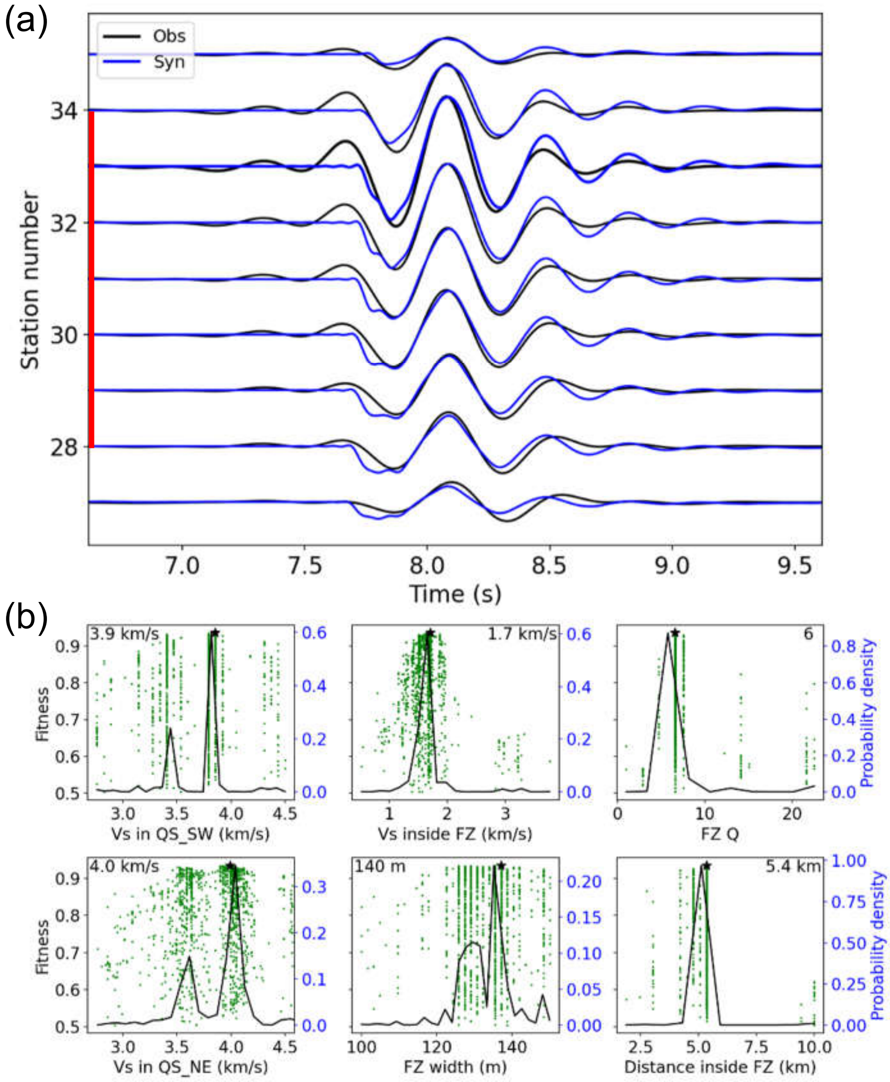

(a)
Obs
Syn
Station number
Time (s)
(b)
3.9 km/s
1.7 km/s
6
4.0 km/s
140 m
5.4 km
Fitness
Probability density
Vs in QS_SW (km/s)
Vs inside FZ (km/s)
FZ Q
Vs in QS_NE (km/s)
FZ width (m)
Distance inside FZ (km)

Figure11.

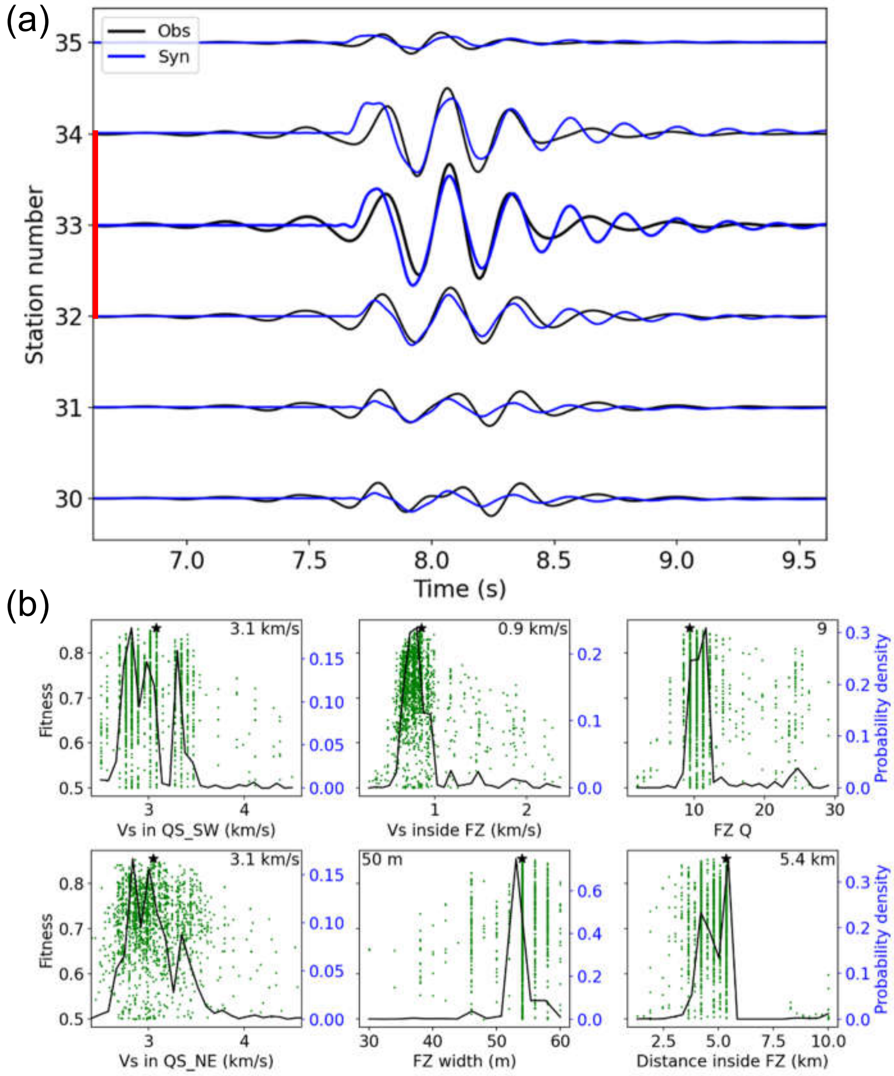

(a)
Obs
Syn
Station number
35
34
33
32
31
30
7.0
7.5
8.0
8.5
9.0
9.5
Time (s)
(b)
Fitness
Probability density
3.1 km/s
Vs in QS_SW (km/s)
0.9 km/s
Vs inside FZ (km/s)
9
FZ Q
3.1 km/s
Vs in QS_NE (km/s)
50 m
FZ width (m)
5.4 km
Distance inside FZ (km)

Figure12.

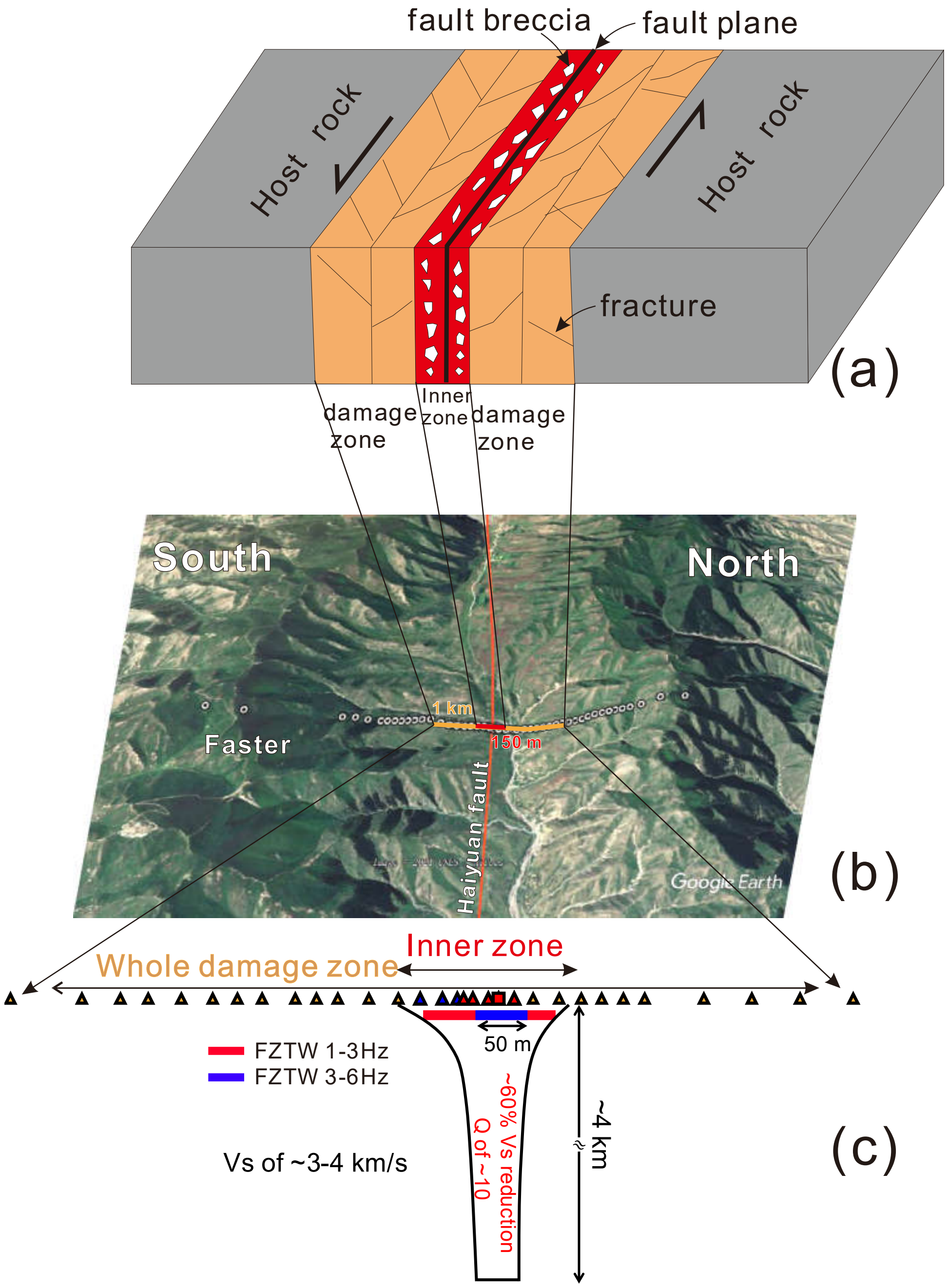

fault breccia
fault plane
Host rock
Host rock
fracture
(a)
damage zone
Inner zone
damage zone
South
North
1 km
150 m
Faster
Haiyuan fault
Google Earth
(b)
Whole damage zone
Inner zone
FZTW 1-3Hz
FZTW 3-6Hz
50 m
~60% Vs reduction
Q of ~10
~4 km
Vs of ~3-4 km/s
(c)